PSFC/JA-05-29

The Magnitude of Plasma Flux to the Main-wall in the DIII-D Tokamak

D. G. Whyte[1*], B. Lipschultz[2], P.C. Stangeby[3], J. Boedo[4], D.L. Rudakov[4], J.G. Watkins[5], W.P. West[6]

1) University of Wisconsin - Madison, 1500 Engineering Dr. Madison WI 53706. U.S.A.
2) M.I.T., Plasma Science & Fusion Center Cambridge, MA 02139, U.S.A.
3) UTIAS, University of Toronto, 4925 Dufferin St. Downsview, ON M3H 5T6, Canada
4) UC San Diego, EBU-II, La Jolla, CA, 92093-0411, U.S.A.
5) Sandia National Laboratories, 1515 Eubank SE, Albuquerque, NM, U.S.A.
6) General Atomics, P.O. Box 85608, San Diego, CA 92186 U.S.A.

Plasma Science and Fusion Center
Massachusetts Institute of Technology
Cambridge MA 02139 USA

December 2005

This work was supported by the U.S. Department of Energy, Grant No. DE-FC02-99ER54512.

The Magnitude of Plasma Flux to the Main-wall in the DIII-D Tokamak

D. G. Whyte[1*], B. Lipschultz[2], P.C. Stangeby[3], J. Boedo[4], D.L. Rudakov[4], J.G. Watkins[5], W.P. West[6]

1) University of Wisconsin - Madison, 1500 Engineering Drive, Madison WI 53706. U.S.A.
2) M.I.T., Plasma Science & Fusion Center Cambridge, MA 02139, U.S.A.
3) UTIAS, University of Toronto, 4925 Dufferin St. Downsview, ON M3H 5T6, Canada
4) UC San Diego, EBU-II, La Jolla, CA, 92093-0411, U.S.A.
5) Sandia National Laboratories, 1515 Eubank SE, Albuquerque, NM, U.S.A.
6) General Atomics, P.O. Box 85608, San Diego, CA 92186 U.S.A.

*Corresponding author e-mail: whyte@engr.wisc.edu

PACS: 52.25.Fi, 52.40.Hf, 52.55.Fa, 52.55.Rk, 52.70.-m

Abstract.

The magnitude of plasma contact with main-wall surfaces is examined on the DIII-D poloidal divertor tokamak. A "window-frame" technique has been developed for axisymmetric surfaces to provide measurements of total plasma flux (ions/s) to the walls, I_{wall}. Despite the use of a separatrix-wall gap that is 2-3 times the radial e-folding length of the plasma parameters near the separatrix, increasing e-folding lengths away from the separatrix result in an I_{wall} of similar magnitude to the ion flux received by the divertor plate, I_{div}. The I_{wall}/I_{div} ratio increases strongly with line-averaged density and ranges from ~0.1-0.2 with attached outer divertor plasmas, to ~ 1 with detached divertor plasmas. These observations hold during core density scans in both low (L-mode) and high (H-mode) confinement energy confinement regimes, and their importance to core fueling and impurities is discussed. It is found that the magnitude of I_{wall} cannot be accurately measured by arbitrary main chamber D-α views due to the strong poloidal and toroidal asymmetry of the plasma contact. However D-α measurements reflect the relative trends of main-chamber recycling. Based on SOL profiles in the shadow of main-wall baffle, the far SOL cross-field particle transport is best described as convective with an effective velocity ~ 100 m/s.

1. Introduction & Motivation

The poloidal divertor is the predominant magnetic topology used for tokamak plasmas. One of the principal functions of the divertor topology is to avoid too strong a plasma-wall contact in the main chamber, which is located close to the core plasma. This is accomplished by redirecting the plasma along open field lines in the SOL (Scrape-Off Layer) to the more remote divertor chamber, which is specifically designed for power and particle exhaust. There are several possible deleterious consequences if the magnitude of plasma contact is too strong at the main-wall: thermal damage of plasma-facing components from conducted heat flux, large impurity release from the walls caused by plasma ion sputtering, and high recycling of neutral hydrogen near the confined plasma leading to loss of fueling control and/or degradation of energy confinement.

In the ideal implementation of a divertor, all heat fluxes that cross the magnetic separatrix, and all charged particle fluxes due to ionizations (inside or outside the separatrix) result in flows along open field lines into the divertor chamber. Most often it has been reasonably supposed that if the gap between the separatrix and the main chamber wall is made sufficiently large, say equal to a few e-folding lengths of SOL n_e and/or T_e near the separatrix, that this would be sufficient to approximately achieve this ideal condition and essentially eliminate the impact of plasma-wall contact outside the divertor. However, recent experiments, from the Alcator C-Mod tokamak [1] and elsewhere, have challenged this view [2-4]. The radial decay length of n_e in the SOL can substantially increase after the initial rapid drop near the separatrix. This suggests that radially extended peripheral plasmas can exist in the "far SOL", leading to significant plasma-wall contact even with relatively large gaps [3]. At the same time, significant evidence has recently been uncovered for the existence of rapid cross-field particle transport in the SOL, particularly as related to intermittent plasma objects moving radially due to **E**x**B** polarization drift (i.e. filament, blobs, etc. see for example [5-8]).

If, as it seems likely, the extended far SOL and this strong convective transport are linked, it is now important to ask the question: what global impact will this transport have on tokamak

operation and design? Answering this question is of great practical importance to the design of future tokamaks like ITER. There exists an important trade-off in choosing the proper gap between the separatrix and main-wall surfaces. It is highly desirable to minimize the gap distance, using as much as possible of the "expensive" magnetic volume for the hot, fusion-reactive plasma inside the separatrix. This must be weighed against the detrimental effects caused by strong plasma-wall interaction that may occur with a small gap. In order to maximize fusion output from a given size of magnetic container, it is necessary to know the size of wall gap that will result in the largest plasma-wall interaction just short of degrading the fusion performance

Obviously, the first step necessary to quantify such "global" questions is to ascertain the total amount of plasma flux to surfaces outside the divertor, herein called 'main-wall' surfaces. Unfortunately, measuring total ion flux to surfaces is made extremely difficult in most divertor tokamaks due to the lack of toroidal and poloidal symmetry oustide the divertor. This stands in contrast to the axisymmetric divertor surfaces where total ion flux is routinely measured.

A variety of methods have been developed and used to measure *localized* radial plasma fluxes which could be used to infer the total flux to the walls. Turbulent transport studies (e.g. [8-10]) utilize a localized measurement (usually with probes) and attempt to connect and extrapolate the underlying turbulence to global particle fluxes. While this helps uncover the underlying transport phenomena across the SOL, it typically suffers from being highly toroidally and poloidally localized within an extensive and probably spatially varying SOL plasma [5,11]. Another concern is the reliability of the measurement itself [7]. Radial transport analysis based on ionization particle balance [4], which provides a time-averaged assessment of transport, is also a localized measurement of radial flux density in the SOL. Such an analysis requires as a boundary condition a separate measurement of the average radial flux density at the limiter radius (the outer boundary of the SOL). That flux density is provided using probe measurements in the shadow region between limiters and is thus an average over the poloidal/toroidal extent of the defining limiter (section 4.1.3 of [3]). Such a transport study of the DIII-D SOL is the subject of the companion paper to this article [12]. Unfortunately, using the average radial flux density between small limiters (i.e. that subtend a small surface area compared to the plasma) in order to

infer the *total* wall flux still requires a large extrapolation. Nevertheless, the limiter plasma flux measurement is attractive: it is a notable improvement over a point measurement with a single probe and it does not rely on local particle balance based on recycling diagnostics.

In this article we develop and extend an experimental method to more accurately measure the time-averaged particle flux to solid surfaces outside the divertor. We coin the term "window-frame" to describe the technique, for reasons that are made apparent in Section 3.1. The primary innovation of this technique is the exploitation of axisymmetric limiter surfaces outside the divertor, so that little or no extrapolation is required in order to measured total plasma-wall flux. The development of the window-frame is an extension of similar experimental method by LaBombard using toroidally localized limiters on C-Mod [4], and theoretical work by Stangeby [13]. In the Appendix, this method is generalized for use with arbitrary axisymmetric surfaces (divertor baffles, centerposts, etc.) with the objective that the technique can be generally applied on other tokamaks. Due to limitations of diagnostic access (rather than a limitation set by the window-frame method) our data are restricted to the low-field side surfaces, but still comprising ~60% of the plasma surface in DIII-D. Obtaining such accurate global particle accounting provides information on how to optimize the plasma and wall geometry with respect to a wide range of issues including impurity control, plasma fuelling, erosion/deposition and tritium inventory. In general, we are interested in exploring the dependence of plasma-wall contact on wall-gap size, main plasma density, confinement mode, etc.

The paper is organized as follows. In Section 3.1, we will exploit unique axisymmetric features of the DIII-D tokamak [14] main-wall geometry and the "window-frame" technique to measure the total plasma flux to main-wall surfaces, I_{wall}, which can be equivalently viewed as the strength of the ion "sink" at surfaces outside the divertor. In Sections 3.2-3.3, I_{wall}, is compared to the particle sinks in the divertor while varying density and energy confinement. We find a strong dependence for I_{wall} on the plasma density, and that I_{wall} is essentially equal to the divertor ion sinks at high density when the divertor plasma detaches. In Section 3.4, our transport analysis of the far SOL plasma profiles in the window-frame shadow suggests a persistent convective-like nature to the radial transport there. In Section 3.5, I_{wall} is compared to the main-wall flux extrapolated from localized recycling measurements (D-α and pressure gauges) in the main

chamber, a commonly employed diagnostic technique for inferring main-wall plasma contact [5,15,16], although one which will be pointed out as problemtatic: .while the trends of main-chamber recycling are well correlated to I_{wall}, the extrapolation of recycling measurements can lead to very large uncertainties (up to a factor of 10) in obtaining the absolute magnitude of main-wall flux, primarily due to the geometric complexity of the plasma contact and accompanying recycling at the main-wall. In Section 3.6, the power exhaust to the main-wall accompanying the main-wall plasma contact is found to be negligible except at the highest densities, where it is still small. In Section 3.7, data are presented on the effect of decreasing the separatrix-wall gap. Section 4 discusses the broader implications of our experimental results on impurity production, power balance and core plasma fuelling and Section 5 contains the conclusions.

2. Experiment description

All results reported in this paper were obtained in deuterium (D) discharges with a diverted, single-null magnetic equilibrium, and $\mathbf{B}\times\nabla\mathbf{B}$ ion drift directed towards the X-point. Detailed information on the tokamak design, diagnostics, and operational characteristics for DIII-D can be found in [14]. A typical equilibrium, vessel cross-sections and diagnostic locations for the experiments are shown in Fig. 1. A photograph of the DIII-D vessel interior surface is shown in Fig. 2. A two-dimensional layout of the SOL plasma, wall geometry and diagnostics is shown in Fig. 3. For convenience we will denote flux surface locations by δ(mm), their outer midplane equivalent separation from the separatrix.

To some, the definition of ‘main-wall’ may be unclear, subjective or arbitrary, and it is important to describe our definition of the main-wall and the reasoning behind it. In this paper we frequently refer to main-wall fluxes, but by this we do not literally mean fluxes equally dispersed to the entire vacuum vessel, but rather fluxes to any “non-divertor” surfaces. Depending on both the geometry of the solid surface and plasma this could be in a wide variety of locations, but typically is to some baffle (or limiter) that “sticks in” toward the core plasma and is installed in the tokamak to protect the vessel and other components. But where do the divertor surfaces stop and the main-wall surfaces begin? There are several potential criteria that can be utilized:

1) As one moves away from the separatrix across flux surfaces, the main-wall begins when the connection length from one divertor to the other is reduced discontinuously and substantially (>10%) due to the interruption of a non-divertor solid surface. This is the most reliable method to define the main-wall since it relies on easily assessed magnetic reconstruction information and is usable with any variety of divertor shaping.

2) The main-walls are those surfaces that reside on the "core" side of the X-point (e.g. above the lower X-point in Fig. 1). This has the benefit of simplicity, but fails to capture information on the variety of equilibrium and divertor shapes possible.

3) The main-wall is connected to those flux surfaces outside of which most of the power is conducted to the divertor. This is sensible for the divertor since it is primarily power that sustains the ionization and recycling occurring there, but it has the disadvantage of being difficult to measure and may change as a result of changes in plasma operation.

For the purposes of this paper we will purposely use magnetic equilibrium where the use of definition 1) is most appropriate. So, for example. in the DIII-D equilibrium shown in Fig.1, portions of the lower divertor outer baffle will be considered as a part of the main-wall even though they are in close proximity to the principal divertor surfaces. This definition is valid since the lower divertor baffle plates are on flux surfaces directly connected to the clearly "non-divertor" upper baffle structures that are receiving the same plasma flux.

In other words, there is no ambiguity as regards to where the divertor surface stops and the main-wall begins at the end of the flux tubes away from the divertor. Plasma streaming along the intercepted flux tube to the sides of the upper baffle (e.g. point A in Fig. 1) constitutes 'plasma on main-wall contact' by any conceivable definition. Even if all the plasma contact occurring at the lower ends of this flux tube (e.g. point B in Fig. 1) is assigned to the "divertor", the amount of plasma-wall contact is only reduced by ~ half. Therefore the definition of the transition from the 'main wall surface' to the 'divertor surface' is not critical to our results.

For the purposes of this paper we will mostly exploit scans in core line-averaged density, $\bar{n}$, at essentially fixed input power, in order to study the main-wall and divertor recycling. Core density is the most convenient control factor for these experiments since it is well known that the edge and divertor plasma recycling flux varies non-linearly (flux $\propto \bar{n}^{2\text{-}3}$) with core density [17].

We will also compare L-mode and H-mode energy confinement regimes. In the present study the wall-gap size is not varied over a great range, but substantial gaps were employed – ~ 2-3 times the SOL e-folding lengths near the separatrix. In future studies, a systematic exploration will be carried out of the effect of varying the wall-gap.

3. Experimental results

3.1. Window-frame technique for plasma flux measurements at the main-wall

Our goal is to determine the net ion flux reaching points radially far away from the separatrix in the SOL, resulting eventually in a total ion "sink" rate to the main- wall surfaces, I_{wall} (ions/s). We base our analysis of I_{wall} on previous work from the Alcator C-Mod tokamak by LaBombard [3] to determine cross-field ion flux density at the limiter radius at the outside edge of the plasma. LaBombard determined the cross-field ion flux density, $\Gamma_\perp$, entering the region between two toroidally *discrete* main-wall baffle surfaces, by integrating the parallel ion current incident on the baffle side faces and invoking particle balance. We have chosen plasma geometries that exploit the fact that several non-divertor surfaces are axisymmetric on DIII-D.. The edges of two toroidally continuous baffles located at the entrance to the upper divertor (labeled A in Fig 1) and lower divertor (labeled B in Fig 1) define a "window-pane" flux surface through which the cross-field ion flux density $\Gamma_\perp \equiv j_{wall}$, (ions s^{-1} m^{-2}), averaged over the window-pane, is passing on its way to the main-wall. The plasma volume residing radially "behind" the window-pane is labeled as the shadow plasma region. The baffle surfaces themselves can be regarded as the "window-frame" and these serve as the plasma ion sinks of the 'main-wall'. From particle conservation, we can relate j_{wall} to I_{wall} by

$$\Gamma_\perp \equiv j_{wall} = \frac{I_{wall}}{Area_{window-pane}} = \frac{I_{wall}}{2\pi R \cdot L_{pol}}, \qquad \text{Eq. 1}$$

where R (m) and L_{pol} (m) are the average major radius and poloidal extent of the window-pane respectively. I_{wall} is essentially independent of any geometry assumption on how the plasma flux is received through the window-pane. Using the axisymmetric window-frames to define and measure I_{wall} avoids the severe problems associated with attempting the equivalent measurement on the non-symmetric surface of the vacuum vessel wall. j_{wall} is the poloidally and toroidally averaged flux density received through the window-pane. While it is likely that the radial ion

flux density is not spatially uniform, j_{wall} nevertheless will provide a useful global comparison for local wall recycling measurements. For convenience we will use the generic term "window-frame" to refer to this axisymmetric arrangement of magnetic geometry and main-wall surfaces, and the main-wall surfaces are referred to as "baffles". By definition the divertor ends, and the main-wall begins, at the window-pane flux surface (Section 2).

Fig. 3 shows a 2-dimensional layout of the boundary plasma and diagnostic locations. Fig. 4 shows a schematic of how the window-frame is used to measure I_{wall}. Figs. 1-3 show several important features:

- Outward moving particles crossing the window-frame flux surface experience a sudden decrease in parallel connection length to solid surfaces.
- While cross-field transport carries plasma through the window-pane surface into the shadow region, the plasma is actually lost to solid surfaces of the window-frame by parallel transport through a sheath (Fig. 4).
- The window-pane is toroidally continuous and its area covers the entire low-field side (LFS) area of the plasma (~60-70% of the total plasma surface area).
- Plasma profiles in the window-frame shadow region can be measured at any toroidal location due to axisymmetry. Both Thomson scattering [18] and a scanning midplane Langmuir probe [19] are used and verified against each other when possible.
- The technique relies solely on plasma diagnosis and not on inferred plasma-wall contact using recycling diagnostics (e.g. D-α emissions).

For further discussion of the window-frame technique, see Figs. 17, 18 and associated text in [13]. We note that the method used in the companion paper [12]- based on particle balance analysis - is most naturally applied to the regions radially inboard of the window-frame. The two methods are thus complimentary with regard to measuring cross-field flux densities, covering different radial regions.

Ideally one would use an array of embedded probes in the window-frame surface to measure directly the incident plasma flux on the window-frames, and therefore obtain I_{wall} from simple spatial integration. However, there is presently only a single embedded probe in the low-field side of the upper baffle of DIII-D (Fig. 1). Therefore, we have developed the methods to obtain

I_{wall} based on plasma measurements in the shadow plasma at locations distant from the window-frame surfaces, taking into account geometry variations and the sink action of the window-frame surface. The details of this methodology are shown in the Appendix. We can summarize the results of the Appendix by showing the dependencies of I_{wall} with fixed magnetic geometry, namely

$$I_{wall} \cong C_{geom} \cdot \left(n_e \ T_e^{1/2}\right)_{window-pane,O} \cdot \lambda_{shadow} \ . \qquad \text{Eq. 2}$$

C_{geom} is a constant depending only on magnetic and window-frame geometry and can be obtained from Eq. A15 in the Appendix. Plasma electron density, n_e, and temperature, T_e, are measured at the window-pane flux surface near the stagnation point, O, generally assumed to be the outer midplane. λ_{shadow} is the fitted radial decay length of the density in the shadow plasma behind the window-frame. Examples of SOL n_e, T_e diagnosis and λ_{shadow} fits are shown in Fig. 5. Note that the magnitude of λ_{shadow} itself is a relative indicator of cross-field plasma transport in the shadow plasma, as will be discussed in Section 3.4.

The magnitude of plasma interaction with the main-wall surface is directly verified on DIII-D by measurement of incident ion flux density using the single fixed Langmuir probe embedded into the axisymmetric upper baffle, which acts as the "upper" section of the window-frame (Figs. 1-3). In Fig. 6, the plasma flux to the probe in the baffle is compared to $\Gamma_{//,i} = \xi\, n_e\, c_s$ (measured on the fixed probe's flux surface) predicted from SOL plasma profiles at locations distant from the baffle surface (Fig. 6) during core density scans (see the Appendix for details on calculating ξ). Agreement is to within 50% over a wide range of line-averaged density and in both L-mode and H-mode plasmas. A possible cause for error is the conservative assumption of $T_i=T_e$ in the calculation of $c_s \propto (T_e+T_i)^{1/2}$. T_i is not directly measured in the shadow plasma, but tends to be ~2-3 × T_e near the separatrix (using charge-exchange recombination spectroscopy). To further complicate matters, it is likely that multiple ion temperature distributions can co-exist in the weakly collisional far SOL. The reasonable agreement shown in Fig. 6 argues that the $T_i=T_e$ assumption is sufficiently accurate. Therefore we expect < 50% systematic uncertainty in the magnitude of I_{wall} (and f_{wall}) obtained by using TS and scanning probe to measure shadow plasma profiles. Overall, Fig. 6 demonstrates a valuable diagnostic check since it directly verifies the magnitude of the plasma flux received at main-wall baffle surfaces in DIII-D.

An assumption underlying the use of the continuity equation in Eq. 1 is that the total ionization rate in the shadow plasma volume must be small compared to the total cross-field flux through the window-pane. If this assumption is incorrect, then by definition j_{wall} will be greater than $\Gamma_{\perp}$ due to the contribution of the ionizations to I_{wall}. While this situation does not affect the accuracy of I_{wall} it can distort the interpretation of j_{wall} with regard to cross-field transport. Fortunately, weak ionization is typically expected for the region behind the window-frame owing primarily to the constant and low $T_e \leq 8$ eV and moderate absolute n_e ($\leq 10^{19}$ m^{-3} on DIII-D) in most cases studied here (see Fig. 5 for example SOL profiles). Based on main chamber gas pressure measurements and the shadow plasma parameters, the ionization source rate in the shadow volume is estimated to be only ~10% of I_{wall}. This relatively small contribution is not surprising since the neutral deuterium ionization mean free-path (MFP) can be estimated to several times larger than the radial dimension of the shadowed region, λ_{shadow}. More detailed studies are planned on the effect of ionization in the shadow plasma.

In the idealized case shown in Fig. 4, the window-frame extends indefinitely in the radially outward direction and all main-wall plasma flux drains to these baffle surfaces. In reality, there exist multiple non-axisymmetric "secondary" window-frames at locations radially further into the shadow plasma - one for each outer midplane bumper limiter, port, etc. For the experiments described here, the primary window-frame is typically separated by ≥ 30 mm $\sim \lambda_{shadow}$ from the midplane limiting surfaces in order to limit the complicating effect of these secondary window-frames.

In our analysis, we will typically compare the low-field side (LFS) main-wall flux to the outer (i.e. LFS) divertor flux. The total ion flux received at the divertor target, $I_{div} \equiv I_{div,LFS}$, is measured using an array of embedded Langmuir probes in the lower divertor [20]. Sweeps of the strikepoints (not shown in Fig. 1) allow all divertor flux surfaces ($0 < \delta < \delta_{window\text{-}frame}$) to be diagnosed with the fixed probes. For convenience we denote the ratio of plasma flux received at the main-wall to that received at the divertor plates as $f_{wall} = I_{wall} / I_{div}$. Our self-imposed LFS analysis limitation arises principally from the lack of SOL plasma profiles on the high field side

(HFS), needed in order to obtain λ_{shadow}. However, this limitation does not greatly affect the accuracy of our accounting of the various ion "sinks":

- The LFS window-pane comprises > 60% of the main plasma surface area.
- The HFS divertor plate receives considerably less incident ion flux due to its detachment at nearly all core densities in the discharges studied here (see Section 3.2).
- It is expected that cross-field plasma transport strongly favors the LFS, due to the effect of bad curvature there [11], this is supported by two experimental results:
    - The HFS embedded probe in the upper baffle (Fig. 1) measures ~4-10 times lower local incident ion flux density than the LFS embedded probe during the same discharge conditions.
    - D-α emissions are ~3-4 times smaller at the HFS than on the LFS of the upper baffle (Section 3.5).

Based on these observations, we conclude that I_{wall} is underestimated by at most 30% due to our lack of HFS diagnostics.

It is important to have a ready, simple basis for making a rough estimate of the importance of plasma-wall contact, and $f_{wall} = I_{wall} / I_{div}$ has the virtue that I_{div} is readily available. However, f_{wall} is not a perfect indicator. For example, in detachment I_{div} can decrease, but some of this decrease is compensated by an increase in volume recombination in the divertor, such that the strength of the total ion sink in the divertor - and thus, in steady state, the strength of the total recycling neutral source – is not solely indicated by I_{div}. A better estimate would be based on the total particle sink in the divertor, however, this is much more difficult to evaluate than I_{div}. In any case, the evaluation of 'bottom-line' questions such as the relative role of wall-recycling and divertor-recycling in the refueling of the confined plasma requires detailed modeling using neutral hydrogen codes such as EIRENE [21], and cannot be done reliably on the basis of any simple indicator. It is evident, however, that when $f_{wall} = I_{wall} / I_{div}$ is of order 1, then plasma-wall contact cannot safely be neglected.

3.2. Main-wall and divertor plasma flux: L-mode

The measurement and comparison of ion sinks, namely I_{wall} and I_{div}, during an L-mode core density scan is shown in Fig. 7. Main-wall plasma fluxincreases strongly with core density: $I_{wall} \propto \bar{n}^3$. In contrast I_{div} "rolls-over" as density increases due to LFS divertor detachment. Therefore, f_{wall} increases strongly with core density. Even at low $\bar{n}$, with an attached divertor, the ratio is substantial, f_{wall} ~0.1-0.2, while $I_{wall} \sim I_{div}$ and $f_{wall} \sim 1$ at the highest L-mode density. These results clearly indicate that the main-wall can effectively compete with the divertor as a plasma ion sink.

The L-mode density scan of Fig. 7 is comprised of repeat discharges in order to obtain complete divertor diagnostic coverage, allowing us to compare other divertor particle sinks/sources to I_{div} and I_{wall}. Both main-chamber and divertor D_2 fuelling were used in these repeat discharges, with no marked difference in SOL profiles, or therefore I_{wall}, between the two cases. The inner (or HFS) divertor plate ion flux, also measured with the divertor probe array, is found to always be less than 30% of the LFS I_{div}, and this fraction decreases strongly with increasing $\bar{n}$ due to the relative ease of detachment at the HFS. The particle sink in the LFS divertor volume due to recombination, I_{rec}, is obtained by interpretation of measured D-γ brightness using calculated "recombinations per photon" ($R/XB(T_e, n_e)$, see [22]). Divertor TS measures $T_e \sim 1$ eV and OEDGE modeling [23] indicates $R/XB \sim 20 \pm 7$ for the $\bar{n} = 4.2 \times 10^{19}$ m^{-3} case. As a result, we infer that $I_{rec} \sim I_{div} \sim I_{wall}$ in "full detachment" at the highest density. It is interesting to note that attempts to raise $\bar{n} > 5.3 \times 10^{19}$ m^{-3} resulted in a radiative limit or "density-limit" disruption. Considering that the unmeasured HFS I_{wall} (estimated to be $\leq 0.25 \times I_{wall,LFS}$, Sec. 3.1) cannot be included in the main-wall plasma flux, we conclude that our restriction to LFS analysis introduces < 25% reduction in f_{wall} (in accounting of *surface* particle sinks). Therefore, the overall uncertainty in f_{wall} remains ~ factor of 50% (see 3.1 and Fig. 6) and f_{wall} appears to be a conservative, but valuable, indicator of the relative magnitude of main-wall plasma contact.

Finally, we find that λ_{shadow} ~30-40 mm, (measured by the scanning probe) has no strong dependence on $\bar{n}$. The non-symmetric "secondary" window-frames (at positions $\delta \geq 100$ mm) therefore reside at least one density e-folding distance behind the primary window-frame (Fig. 3), implying that the symmetric baffles (points A and B in Figs. 1-2) are the regions of most intense main-wall plasma interaction.

3.3. Main-wall and divertor plasma flux: H-mode

The measurement of I_{wall} and I_{div} is complicated by the presence of Edge Localized Modes (ELMs) in H-mode energy confinement regimes. From Fig. 8 we see that a type-I ELM causes a sudden burst of incident plasma ion flux to appear at the main-wall. However, *we note that the quantitative and causal link between local main-wall surface recycling and plasma flux is not broken by the L-H transition, nor during ELMs* (further discussed in Section 3.5). The embedded probe measurement indicates that ELMs are the cause of 30-40% of the time-averaged localized incident ion flux density to the window-frame., Similarly, ~40% of outer divertor D-α emissions is accounted for by ELMs.

An accurate assessment of the type-I ELM particle flux received at the main-wall and divertor surface is not presently possible. In the divertor, the ELMs saturate the embedded Langmuir probes and D–α interpretation is made inexact by the unknown plasma parameters (T_e, n_e) during the ELM. At the main-wall we presently have no method to determine λ_{shadow} during the type-I ELM and therefore we cannot accurately obtain I_{wall}. A further diagnostic concern is the poloidal localization of the ELMs. It is clear that any study of plasma particle transport in H-mode that does not include ELMs is necessarily incomplete. However, we note that an embedded array of radially displaced Langmuir probes continuously collecting ion saturation current in the window-frame baffle surfaces would provide a relatively simple way to measure temporally-resolved I_{wall} caused by ELMs, although it may be necessary to place such arrays at multiple toroidal locations due to the ballooning characteristic of the ELMs.

We first examine fluxes in the case of an H-mode obtained with the same plasma geometry described in the previous section (Fig. 1). This H-mode is characterized by the accompanying type-I ELMs and an attached outer divertor (case $\bar{n}$ ~6.3x10^{19} m^{-3} in Fig. 7). In this case, the ELM contribution to H-mode I_{div} and I_{wall} is estimated by assuming: 1) The relative divertor ELM D-α contribution correctly provides the relative ELM flux contribution, 2) That λ_{shadow} does not change substantially from its intra-ELM value of ~30 mm and 3) the ELMs originate at the LFS SOL. The constant λ_{shadow} during an ELM is conservative since λ_{SOL} broadens during an

ELM on DIII-D [24]. The total magnitude of edge plasma particle flux is clearly reduced in H-mode compared to the L-mode (Fig. 7). This is an expected consequence of the improved *global* particle confinement associated with H-mode. However, we further note that the f_{wall} is essentially the same as in an attached L-mode, i.e. the relative importance of main-wall plasma flux is not less in H-mode than in L-mode. The H-mode reduction in particle transport apparently affects the divertor and main-wall regions by the same magnitude.

We have applied the same analysis techniques described above to a high-triangularity, upper single null H-mode with a core density scan controlled by main-chamber D_2 fuelling (Fig. 9). This discharge was characterized by much smaller amplitude, more rapid ELMs than the H-mode case described above. *This allowed us to use time-averaged TS main-plasma SOL profiles and divertor probe analysis that includes the effect of the ELMs in a time-averaged manner*. In this geometry, the main-wall baffles forming the window-frame are the upper outer divertor baffle and the "corner" of the axisymmetric inner wall located near the bottom, left quadrant of the wall (locations A and B in Fig. 9). The first flux surface contacting these limiting surfaces is at $\delta \sim 40$ mm and the window-pane subtends ~75% of the main plasma surface area. We note that this particular window-frame geometry, which exploits an axisymmetric inner wall, is more likely to be available on other tokamaks. Accurate measurements of I_{wall} would therefore be possible with appropriate distancing of the separatrix from non axisymmetric surfaces, measurements of plasma profiles in the shadow region and proper calculation of C_{geom} (Eq. 1) based on the derivations given in the Appendix.

As in the L-mode case, we find a strong dependence for the fluxes on $\bar{n}$ and detachment. For the attached divertor phase, $\bar{n} < 8\text{x}10^{19}$ m^{-3}, $f_{wall} \sim 0.25$, while for a high-density detached divertor, $f_{wall} \geq 1$. An indication of the intense plasma main-wall contact is that for $\bar{n} \sim 9\text{x}10^{19}$ m^{-3} the incident Γ_i on the embedded probe at the upper divertor baffle actually surpasses Γ_i at the divertor target strikepoint, and the n_e plateau in the far SOL ($\delta > 30$ mm) is ~ 2-3x10^{19} m^{-3}, a density more typical of a divertor plasma. Similarly to L-mode, we find $\lambda_{shadow} \sim$ 40 mm, and that λ_{shadow} is relatively constant vs. $\bar{n}$.

3.4. Interpretation of λ_{shadow} for plasma transport

The shadow plasma as shown in Figs. 2-3 is a good example of a" simple SOL" (see Chapter 1 of [25]). Cross-field transport "fills" the shadow plasma (in this case from the principal SOL) with little ionization occurring within its volume. The competition between cross-field (or radial) and parallel transport to the end baffles then sets the characteristic radial scale length for the plasma, namely λ_{shadow}. For diffusive-like transport, the effective diffusion coefficient is given by

$$D_{eff} \approx \frac{2\lambda_{shadow}^2 c_s}{L_{//}} \text{ (m}^2\text{ s}^{-1}\text{)}, \qquad \text{Eq. 3}$$

where $L_{//} \sim L_{pol} \bullet (B_T/B_Z)|_{midplane}$ is an effective parallel connection length between the two main-wall baffles for λ_{shadow} mapped to the outer midplane. For convective-like transport, the convection velocity is given by

$$v_{eff} \approx \frac{2\ \lambda_{shadow}\ c_s}{L_{//}} \text{ (m s}^{-1}\text{)}. \qquad \text{Eq. 4}$$

Here we use $c_s \sim (kT_e + kT_i / m_D)^{1/2} \sim 2.5\text{x}10^4$ m/s by taking $T_i=T_e\sim$7 eV in the shadow plasma (Fig. 5).

The resulting transport coefficients are summarized in Table 1. We notice that D_{eff} is ~ 10-40 times larger than the Bohm diffusion coefficient $D_{Bohm}= k\ T_e / 16\ e\ B \sim 0.2\ m^2\ s^{-1}$ in the shadow plasma. This suggests that the diffusion ansatz is likely inappropriate for the far SOL and shadow plasma. On the other hand, the time-averaged $v_{eff}\sim$100 m/s is in good agreement with far SOL particle balance measurements [12], transport modeling [16], and ExB fluctuation driven transport based on probes taking into account the ~25% fluctuation levels [9][26]. Therefore the convective transport ansatz seems more appropriate here. It is interesting to note that there is little difference in λ_{shadow}, and hence D_{eff} or v_{eff}, between the L-mode and H-mode cases. There does not appear to be any significant dependence of λ_{shadow} on <n> either, again consistent with C-Mod measurements [4]. This is in contrast to the expected L-H reduction in global, and near-separatrix, transport coefficients, and suggests that the particle transport mechanism in the far SOL is de-coupled from the physics governing H-mode near the pedestal and separatrix.

3.5. Neutral recycling at the main-wall

To this point analysis has been limited to main-wall plasma contact and plasma-based diagnosis. An obvious consequence of plasma main-wall contact is the accompanying source of recycled D molecules and neutrals from the main-wall, leading to plasma fuelling. The D neutral influx, Γ_D (D m^{-2} s^{-1}), is inferred at discrete main-wall locations using both pressure gauges and D-α brightness. The gas pressure, typically ~10^{-4} Torr in the main chamber for these experiments, is interpreted as a D_2 ($\Gamma_{D2} = 1/4\, n_{D2}\, \bar{v}$) molecular flux density (assuming room temperature D_2 molecules from the DIII-D wall), of which half the flux travels toward the plasma and contributes to local D atom ionization in the plasma after molecular dissociation, i.e. $\Gamma_D \sim 2$ (D/molecule) x 1/2 Γ_{D2}. For D-α views approximately normal to recycling surfaces (e.g. the baffle views in Fig. 1), the D–α brightness, $B_{D-\alpha}$ can be directly interpreted as D atom influx using the well-known ionizations per photon ratio (S/XB~20 for D-α) ratio, i.e. $\Gamma_D \sim 4\pi\, B_{D-\alpha}$ S/XB [27]. This simple interpretation is possible because the deuterium atoms are ionized and excited in the same viewing volume. The case is somewhat different for the midplane D-α array, since it does not directly view a recycling surface but rather has viewchords tangent to the SOL (Fig. 1). Here one must invert the measured brightness profile to arrive at a radial emissivity (photons/m^3) profile, which is then converted to a volumetric ionization profile (ionization/m^3) using S/XB based on local n_e and T_e. The ionization profile is then radially integrated through the SOL to arrive at a local, outer midplane Γ_D.

In Fig. 10, the main-wall D recycling fluxes, Γ_D, measured at various locations at the LFS main-chamber are compared to the averaged plasma ion flux density to the main-wall, j_{wall}. Since $j_{wall} \equiv I_{wall} / A_{window\text{-}pane}$, we can view this as a test of the accuracy of extrapolating local recycling measurement, i.e. Γ_D x $A_{window\text{-}pane}$, for measuring main-wall plasma contact. We first note that all of the measurements of Γ_D are strongly correlated in their relative magnitude with j_{wall} as $\bar{n}$ increases. However the absolute *magnitude* of local recycling does not agree with j_{wall} and is not consistent among the different locations. This illustrates the complications in the poloidal and toroidal pattern of the received plasma flux and accompanying recycling from the main-wall surface. Beyond the axisymmetric baffles (Fig. 3) that define the window-frame the details of the spatial distribution of the plasma-wall interaction are complicated and unknown. Therefore, *local* main-chamber D recycling cannot be used to determine accurately the *absolute magnitude* of the total plasma flux to the main-wall surface**.** However, if the radial plasma transport mechanism in

the shadow region is nearly constant with different plasma conditions (which it is as indicated by constant λ_{shadow}~40 mm), then the *relative* fraction of total D main-wall recycling occurring at any arbitrary (toroidal and poloidal) main-wall surface should *correlate* to I_{wall}. *The relative magnitude at each main-wall location is related to its specific window-frame location in flux space*. Therefore, main-wall recycling diagnostics provide a useful method for measuring the *trends* of plasma contact outside the divertor. However a simple expectation is met, in that the local recycling flux is much larger at the primary window-frame surface themselves (i.e. 'A' and 'B' in Fig. 1,) than at the non-axisymmetric midplane surfaces that reside further out in the SOL. *Therefore the actual location of main-chamber recycling is highly dependent on plasma and wall geometry*.

The magnitude of the midplane Γ_D, (based on midplane D-α and pressure gauges), the measurement of which are distributed at different toroidal locations, turns out to be quite close in absolute magnitude to j_{wall} (Fig. 10). This might be expected for the pressure gauges that tend to average out the local recycle flux density due to their remoteness from the edge plasma. However, the factor of ~2 agreement between midplane D-α Γ_D and j_{wall} appears *purely coincidental* given the complicated role played by the three outer midplane bumper limiters (Fig. 1-2). Interestingly, this fortunate coincidence tends to validate the global SOL transport analysis of Pigarov et al,, that was based largely on the DIII-D outer midplane D-α array [16], but does not validate in general the use of midplane D-α signals for main-wall plasma interactions We further note that D-α brightness from the HFS of the upper baffle (Fig. 1) is about a factor of three smaller than from the LFS (Fig. 10). This is a qualitative indication of the expected weaker radial transport at the HFS, also consistent with the transport analysis of [16].

Our measurements of I_{wall} and Γ_D are also consistent with the recent observations of Groth et al. who found the midplane main-chamber D-α for the lowest density, $\bar{n}=2.5\text{x}10^{19}$, L-mode condition (Section 3.2) to be very weak compared to the divertor [28]. Based on our measured f_{wall}, ~0.1, (Fig. 7) and taking into account the large flux expansion (factor of ~7) from the midplane to the baffle, we expect *local* recycling flux density, Γ_D at the divertor to be ~70 times larger than the Γ_D at the window-frame baffles, and > 200-500 times the recycling flux density at the midplane locations (compare Γ_D's in Fig. 10). This example illustrates the inherent

difficulties associated with inferring main-wall plasma contact using the diffuse and non-uniform D-α emissions from the complicated surfaces of the main chamber, particularly in the presence of divertors with strong local recycling.

The strong non-uniformity in main-wall recycling, Γ_D, means that the absolute magnitude of the total neutral influx fuelling the plasma (I_D) is very difficult to determine accurately over the toroidal and poloidal extent of the window-frame, even with the extensive D-α coverage in DIII-D. Because of the excellent correlation between j_{wall} and Γ_D it is initially tempting to assign all of the main-chamber neutral influx and fuelling to j_{wall}. However we must allow that neutral leakage from the divertor might play some role in the neutral gas fuelling in the main plasma's SOL. With this in mind we note two empirical observations that indicate *against* the importance of divertor leakage dominating the measurements of Γ_D. First, Fig. 8 shows a direct confirmation that plasma contact at the main-wall is the dominant cause of refueling and ionizations in the SOL plasma near the baffle surfaces. *The D recycling flux follows very closely the magnitude and trend of incident plasma flux at the same surface. This is exactly as one would expect for the saturated graphite surfaces recycling the incident ion flux as neutral D.* This comparison, which necessitates an embedded probe in an axisymmetric surface, is only available at location A for the plasma shape used (Fig. 1). Secondly, approximate up-down symmetry in Γ_D is found in the trends comparing the LFS upper baffle (point A, Fig. 1) and lower baffle Γ_D (point B) (see Fig. 10). This symmetry is obviously consistent with plasma-wall caused Γ_D since the two baffles intersect the same flux surface.

The presence of D gas and recycling far outside of the divertor has often been attributed to leakage of divertor recycled neutrals, a complex process which can only be assessed indirectly, through modeling (see for example [29]). More recently an experimental assessment of the divertor leakage showed it to make a small contribution to the midplane neutral population in Alcator C-Mod [4]. The results in this paper indicate no significant role for, or need to invoke, divertor leakage as the cause of recycling far from the divertor, since plasma transport to the main-wall appears of sufficient magnitude and trend to explain the D recycling at these locations. Note that this study cannot, however, rule out the role of leakage near the active X-point or along the inner divertor leg (which is not diagnosed in this study).

We can also make more speculative remarks supporting our hypothesis of direct linkage between I_{wall} and the inward flux of neutrals. The main-wall D recycling, Γ_D, does not correlate with the received ion flux at the divertor targets, I_{div}. This is apparent in comparing Fig. 7 and Fig. 10: I_{div} drops due to detachment whilst j_{wall} and Γ_D continue to increase with $\bar{n}$. It seems unlikely (though admittedly not impossible) that the divertor "shielding" of neutrals would adjust in precisely the manner, along with the complications arising from volume recombination, which would be required to make the leakage rate exactly correlate with j_{wall} and Γ_D. There is no apparent feedback mechanism between the divertor particle sink (both in the plate and through volume recombination), divertor shielding and j_{wall} that would cause such a scenario to occur. This is an issue that might be addressed by modeling but is beyond the scope of this paper.

Therefore based on the foregoing empirical observations, we conclude that plasma flux to the main-wall, i.e. I_{wall}, plays the dominant role in determining the D refueling at the LFS main plasma SOL away from the X-point.

3.6. Power balance and main-wall plasma flux

Power balance is an important and useful check on the validity of the magnitude of I_{wall}. We apply the standard sheath theory to determine Q(W), the power extracted through the sheath caused by the plasma-wall interaction. For the main-wall

$$Q_{wall} = \zeta \cdot kT_{e,shadow} \cdot I_{wall}, \quad \text{Eq. 5}$$

and for the divertor,

$$Q_{div} = \zeta \cdot kT_{e,div} \cdot I_{div}, \quad \text{Eq. 6}$$

where ζ =7 is the typical sheath energy transmission coefficient [25]. We use the measured average value of $T_{e,shadow}$~ 6 eV, and the divertor plate $T_{e,div}$ as measured by divertor TS. The estimated uncertainty in Q_{wall} is ~50%.

Fig. 11 shows power balance results in the L-mode density scan (Fig. 7). The sheath-conducted power losses (Q_{wall}, Q_{div}) and total (divertor and core) radiated power loss (P_{rad}) are compared to the input heating power (ohmic and neutral-beam heating). At low density, with an attached

outer divertor, Q_{wall} is small. This implies a small portion, ~2-3%, of the exhausted power is due to plasma main-wall contact. Indeed when the divertor is attached, the power exhaust is concentrated in regions near the strikepoint (higher T_e and heat conductivity) and Q_{div} accounts well for P_{in}-P_{rad}. (We have neglected the small Q contribution from the inner divertor target). Since $Q \propto T_e$, from Eqs. 5-6, Q_{wall} is ~20-30 times lower than Q_{div} in the attached L-mode ($T_{e,div}$ > 20 eV), although I_{wall}/I_{div} is ~ 0.1 – 0.2.

However Fig. 11 shows that Q_{wall} becomes increasingly significant in the power balance as $\bar{n}$ increases and the divertor detaches (at $\bar{n}$>4x10^{19} m^{-3}, Fig. 7). The main-wall plasma contact, Q_{wall}, provides ~10% of the exhausted power, the remainder being provided by volumetric radiation. Simultaneously, heat conduction to the divertor target is essentially absent due to detachment ($T_{e,div}$ < 2 eV). This is consistent with global power balance within the measurement uncertainty. At high $\bar{n}$, 40% of the radiated power emanates from outside the divertor. Therefore in L-mode detachment, ~50% of the power exhaust occurs outside the divertor volume, primarily reaching the walls as radiation.

3.7. Effect of decreasing the separatrix to window-frame gap

We have examined the effects on I_{wall} and I_{div} made by decreasing the gap between the separatrix and the window-frame, $\delta_{W.F.}$, from 60 mm to 25 mm (Table 2). This was accomplished in a controlled manner by decreasing the distance between the top of the core plasma and the axisymmetric upper window-frame, such that point A in Fig. 1 resided at the δ=25 mm flux surface. The gap size normalized to the plasma minor radius is thus reduced from ~11% to 4.2 %, while the core plasma volume increased by ~15% and q_{95} increased by ~21% (3.8 to 4.6). The decrease in gap had no discernible effect on global plasma parameters such as energy confinement, which is expected since total plasma current was kept constant. The midplane bumper limiter surfaces are positioned at δ~70 mm, at least one e-folding distance, λ_{shadow}~30 mm back from the primary axisymmetric window-frame. The small top gap pushes TS points out of the SOL, such that only the midplane scanning probe can be used for the I_{wall} SOL profile measurements. Our limited gap-scan dataset presently restricts us to examining the effects at a single plasma condition: L-mode, $\bar{n}$~3.6×10^{19} m^{-3} (Section 3.2, Fig. 7).

Table 2 shows that the ~60% reduction of $\delta_{W.F.}$ results in about a 4× increase in I_{wall}. The increase in I_{wall} is confirmed by a 4× increase in Γ_t, the local received ion flux density at the embedded probe in the window-frame (Table 2 and Fig. 6). This relative increase can also be roughly estimated from the SOL profile taken during the reference case (arrows on Fig. 5): the parallel ion flux density ($\propto n\, T^{1/2}$) increases a factor of ~4 between the $\delta_{W.F.}$~ 60 mm and δ~25 mm flux surface. This suggests that the effects of gap distance on I_{wall} can be roughly scaled based on the SOL profiles taking with relatively large gaps (such as Fig. 6), as long as λ_{shadow} remains constant. Indeed, λ_{shadow} does not significantly change with the decreasing gap (Table 2), again suggesting that the far SOL radial transport is roughly constant and convective with v_{eff} ~ 100 m s^{-1} (Section 3.4). Therefore, one might expect a weaker effect on I_{wall} vs. gap distance at high line-averaged density; the SOL density profiles become increasingly flat versus δ, and increasing $\delta_{W.F.}$ may not significantly reduce I_{wall}. This observation may have significant implications on the choice of the "optimal" gap, but needs more detailed experimental exploration.

I_{div} decreases slightly, by ~20%, with the reduced gap (Table 2). *The smaller gap therefore results in a five-fold increase of f_{wall} from ~0.1 to ~ 0.5*. The relative importance of the main-wall ion sink generally increases with decreasing $\delta_{W.F.}$, and the details of plasma-wall gap play an important role in determining f_{wall}. This observation may help to explain why f_{wall} is higher in the H-mode case studied here ($\delta_{W.F.}$~40 mm, Fig. 9) than the L-mode (($\delta_{W.F.}$~60 mm, Fig. 7).

Decreasing the wall gap also increases the power sink at the main-wall: the ratio of conducted power to the window-frame, Q_{wall}, to the total power into the divertor, P_{div} ($=P_{rad,div}+Q_{div}$) increases seven-fold from ~3.5% to 27% (Table 2). The increase in Q_{wall} is caused by both the increase in I_{wall} and the increase in average T_e at the window-frame flux surfaces. The increase of Q_{wall} / P_{div} to 27% is consistent with the new location of the window-frame moving to just outside the e-folding power width ~ 20 mm (see T_e profile in Fig. 5), if one reasonably presumes that cross-field convection is responsible for Q_{wall}. It is further interesting to note that Q_{wall} / P_{div} ~ 27% is roughly consistent with the ~22% reduction in the magnitude of I_{div}, the divertor ion sink; suggesting that the divertor particle recycle loop is primarily sustained by power transfer to the divertor rather than particle transfer from the core SOL (since f_{wall}~0.5 > Q_{wall} / P_{div}). All in all,

this study indicates that the non-divertor surfaces can begin to become a much more significant particle and power sinks as the gaps decrease. The increasing influence of the wall comes with the benefit of increasing the confined plasma volume (+15% in the case studied here, Table 2), so the choice of gap can be seen to be critical to overall plasma performance.

4. Discussion: Implications of main-wall plasma flux

The results of this paper have implications for main chamber recycling. The measured magnitude of the plasma flux to the main-wall, I_{wall}, as well as the relative ratio of main-wall flux to divertor flux, $f_{wall} \sim I_{wall}/I_{div}$ show that this flux is generally important on DIII-D in both in L-mode and H-mode. More window-frame experiments are needed to expand the variety of discharge type and plasma-wall gaps, and to better assess the role of transients like ELMs on main-wall particle and heat loads. Also needed are further comparisons of the various transport analysis techniques - window-frame, particle transport and turbulent transport analysis.

The magnitude of I_{wall} (and f_{wall}) increases strongly with core plasma density, $I_{wall} \propto \bar{n}^3$. This trend is generally consistent with the combination of a constant convective-like transport in the far SOL (v_{eff} ~100 m s^{-1}, Section 3.4) and the expected non-linear relationship of SOL density with core density ($n_{SOL} \propto \bar{n}^{2-3}$ [17]), since the convective flux density scales as $\Gamma \sim n_{SOL}\, v_{eff}$. The onset of divertor detachment at high $\bar{n}$ decreases I_{div}, thus making the main-wall surfaces a relatively larger ion sink. However, this picture is likely too simple, since I_{wall} itself plays an important in refueling the plasma, and therefore the role of neutral refueling and particle transport must be considered more self-consistently to properly address these issues. The trend of SOL transport and fueling versus $\bar{n}$ are discussed in greater detail in the companion paper on scaling studies between DIII-D and Alcator C-Mod [12].

While main-wall fluxes are important in current tokamaks, it is not so clear how these fluxes scale to a burning plasma experiment like ITER. It is first necessary to better understand the underlying physical processes controlling I_{wall}. Comparisons have begun of turbulence measurements and global recycling measurements across different devices, and this should allow for accurate dimensionless similarity scaling studies. The initial results from the latter indicate

that the strong cross-field, convective-like transport in the far SOL is essentially the same across C-Mod, JET and DIII-D [12,30]. This scaling and the empirical trends noted in our experiments raise potential concerns for a device like ITER [31] which: 1) Will operate at large normalized density near the empirical Greenwald density limit with a detached divertor ($\bar{n} \sim 10^{20}\,m^{-3}$, $n_{separatrix} \sim 3\times10^{19}\,m^{-3}$) implying a far SOL collisionality similar to present experiments, 2) Will have a relatively small plasma-wall gap normalized to plasma minor radius a_{plasma}, $\delta_{W.F.} / a_{plasma} \sim 40$ mm / 2 m ~ 2%, in comparison to $\delta_{W.F.} / a_{plasma}$ ~10% used in DIII-D, and 3) Will produce many dimensionless plasma parameters in the far SOL that are similar to present experiments (e.g. ν^*, β^*) while others are not (e.g. ρ^*) [12,30]. Clearly, further experiments and transport studies are required to provide reliable extrapolation of our present experience with main-wall plasma contact to future larger devices like ITER. Such an accurate extrapolation will help improve the design of first-wall and divertor components, in order to improve both the reliability and lifetime of the components, and to achieve the overall goals of particle fuel, ash and impurity control that are necessary in a burning plasma.

In the following three sub-sections we discuss the impact of main-wall plasma flux for DIII-D.

4.1. Impurity sources and core contamination

An obvious consequence of I_{wall} is the release of impurities due to sputtering at the main-wall. The sputtering occurs due to the ion flux associated with I_{wall}. Ions are accelerated through a sheath determined primarily by T_e. Significant ion bombardment energy, and therefore the potential for substantial sputtering yield, is then expected at the main-wall. For DIII-D carbon tiles, we expect both chemical and physical sputtering, with total yield C/D^+~1-2% to occur at the main-wall and the divertor surfaces. The D ions may be just above the physical sputtering threshold ($E_{D+} \sim 5\,T_e > E_{threshold} \sim 20$ eV) at the main-wall, and the chemical erosion will be strong due to its weak ion energy dependence. Significant chemical erosion yields, ~1%, have been measured spectroscopically at the DIII-D main-wall surfaces [32].

An examination of the carbon radiation patterns during the L-mode density scan (Sec. 3.2 and Fig. 7) clearly confirm the link between increasing I_{wall} and main-wall carbon influx as $\bar{n}$

increases (Fig. 12). Visible C^{+2} brightness is an approximate indicator of local carbon sources / ionization. C^{+2} brightness from the upper baffle and the outer midplane increase as $\bar{n}^2$, while the divertor C^{+2} brightness is flat with $\bar{n}$ as the divertor detaches. Likewise, total radiated power increases as $\bar{n}^3$ in the SOL near the upper baffle away from the divertor, but trends to a constant value in the divertor. Taking into account the larger surface area of the main plasma, the comparable magnitudes of C^{+2} brightness and radiated power suggest that the carbon source has even become somewhat larger than the divertor source at the higher densities. Further work on properly quantifying the distributed carbon source from the main-wall, for example including the effects of ionization/photon efficiency, is underway.

If total carbon influx is similar over the main-wall and divertor surfaces, what relative role do we expect I_{wall} to play in setting the level of core impurity contamination? To answer this question requires additional knowledge of impurity transport. Impurity injection experiments have typically found much higher penetration probability, $P \sim \Delta N_{core}/N_{injected}$, from main-wall surfaces than from divertor surfaces [33-36]. This result meets our dual expectations that the divertor plasma shields impurities effectively and that the impurity released from the main-wall has much easier "access" to the core plasma. Recent experiments on DIII-D showed that hydrocarbon molecules (a simulation of chemical sputtering) launched from the main-wall had at least a 10-fold higher core penetration probability, i.e. $\phi \sim P_{main\text{-}wall}/P_{div} > 10$, than those launched from the divertor [37].

On DIII-D, the main-wall carbon source caused by I_{wall} is then expected to be a major determining factor in core plasma carbon contamination, since $\phi \cdot f_{wall} \geq 1$. Note this appears to be the case at all $\bar{n}$ studied (Fig. 7) and in both L-mode and H-mode (Fig. 9) where $f_{wall} \geq 0.1$. In full detachment, when the $f_{wall} \sim 1$ and $\phi \cdot f_{wall} \sim 10$, the main-wall source may completely dominate the impurity sources and the core plasma contamination. This conclusion is not strongly affected by the fact that we are basing f_{wall} on I_{div}, rather than total divertor particle sink , since impurity production is governed chiefly by I_{div}. This is consistent with observations of carbon net deposition at all divertor locations in detached plasmas in DIII-D [38] , implying a net main-wall source external to the divertor. It is important to note that the role of main-wall plasma

flux could be dramatically different if another plasma-facing material is used, especially if incident ion energy falls below the sputtering threshold at the main-wall.

4.2. Power exhaust and divertor conditions

The power drained by I_{wall} to the main-wall surfaces, is an almost negligible component in heat exhaust with attached divertor plasmas (Sections 3.6). It is expected that an attached divertor with significant parallel heat conductivity ($\propto T^{5/2}$) is the primary sink of the SOL heat conduction. Indeed, it is understood that the divertor is primarily sustained by strong parallel heat transport in the SOL, while its parameters are determined via local self-consistency (recycling, T_e, n_e, etc.) [25]. *It is therefore satisfying to note that there is no fundamental inconsistency between the record of successful understanding and diagnosis of divertor plasmas* [17,39,40] *and the existence of substantial main-wall plasma interaction.*

In detached plasmas, or with smaller wall-plasma gap, the role of cross-field heat transport to the wall is relatively more important, comprising ~10-15% of the input power (Sections 3.6-3.7). This could be important for burning plasma experiment like ITER, where some degree of detachment is envisioned in order to control the divertor heat flux. It is possible that the detachment "solution" simply moves several of the problems associated with plasma exhaust (wall erosion, impurity control) to the main-wall – which is possibly ill-suited for such interaction (e.g. a beryllium wall). The causal role of the I_{wall} and Q_{wall} in *inducing* detachment, or vice versa, is unclear, since to date detachment has been explained primarily on the basis of parallel SOL physics. Presumably the fact that Q_{wall} is non-zero reduces the value of $\bar{n}$ at which detachment sets in, for a given power input. However, the relatively low fraction of power lost to the main-wall at the onset of detachment would be a minor perturbation to these models.

4.3. Core plasma fuelling

It is expected that the D recycled from the main-wall has better geometric "access" to the core plasma than divertor recycling neutrals, as is the case with impurities (4.1). Also, it was experimentally determined that divertor (private-flux region) deuterium injection was 2-3 times

less efficient than main-chamber D injection at maintaining core density for the L-mode cases studied in 3.2. Therefore we expect that even a modest ratio of main-wall to divertor flux ($f_{wall} \geq 0.2$ as measured) will have a significant impact on core fuelling, and potentially on the formation of the density pedestal..

The magnitude of the main-wall refueling loop is I_{wall}, since by definition this describes a closed particle loop with the main plasma and SOL. I_{wall} can then be compared with the core-refueling loop that originates in the divertor via X-point fuelling or divertor leakage. This fueling loop must close by particle SOL transport "draining" back into to the divertor, I_{drain} (see for example the graphical representations of particle loops in [12]). Therefore a comparison of I_{wall} with I_{drain} indicates the relative importance of main-wall recycling and core fueling – at least for attached divertor conditions (see previous discussions of neutral recycling due to volume recombination in detached divertor plasmas). One can roughly estimate I_{drain} by integrating toroidally the local flux density drainage ~ $M\, n_e\, c_s$ across the width of the SOL, and neglecting ExB drifts. As an example, $I_{drain} \sim 10^{22}\ s^{-1}$ for the L-mode $\bar{n} = 3.5 \times 10^{19}$ case (Fig. 7), with sub-sonic flow, Mach number M ~0.2, taken from Mach probe measurements located 40 mm outboard of the X-point, well inside the 1 cm outer midplane equivalent flux surface. The resultant I_{drain}/I_{div} is ~ 0.2, indicative of the expected flux amplification in the divertor. Therefore since f_{wall} ~ 0.1-0.2 we find that $I_{drain} \sim I_{wall}$. *Therefore the main-wall recycling fuelling loop and the divertor fuelling loop are of a comparable magnitude with regard to the plasma outside the divertor*. We further note that the fact that $I_{drain} \sim I_{wall}$ is consistent with the high efficiency of divertor pumping in DIII-D to reduce core density: there remains an important fuelling loop that circulates through the divertor, at least in this attached plasma case studied. Also, since the pumping rate is always small compared with either I_{wall} or I_{div}, a quite small value of I_{drain}/I_{wall} can be sufficient for pumps in the divertor region to control the density in the main plasma.

5. Conclusions

Plasma and recycling diagnostic techniques have been applied to the edge plasma region of the DIII-D poloidal divertor tokamak in order to assess the magnitude and trends of plasma contact with the main-wall surfaces outside the divertor. Wall-gaps were employed of 60 mm and more,

which is large (x 2-3) compared with the SOL e-folding lengths near the separatrix. The plasma ion flux received by main-wall surfaces, I_{wall} is typically a significant fraction of the ion flux at incident on the divertor plate, $I_{divertor}$. The $I_{wall}/I_{divertor}$ ratio increases with line-averaged density and ranges from 0.1 with attached outer divertor plasmas, to ~ 1 with detachment. The ratio of I_{wall} to the flux draining into the divertor, I_{wall}/I_{drain}, is even larger, of order unity and larger. These observations hold during core density scans in both low (L-mode) and high (H-mode) confinement energy confinement regimes. Therefore, even when employing substantial wall-gaps, DIII-D experiences main-wall plasma interactions that are always significant for plasma refueling and impurity production. The main-wall interaction becomes dominant in high-density detached plasma operation. The inferred power removal via plasma on main-wall contact is negligible with attached divertors, but comprises ~10% of input power at full detachment, consistent with global power balance.

Acknowledgements

The authors wish to acknowledge the essential contributions of the DIII-D experimental team.. Helpful discussions with B. LaBombard, T. Taylor and A. Leonard are also acknowledged. This work was supported by the U.S. Department of Energy under Grant No DE-FG02-04ER54762, Cooperative Agreement No. DE-FC02-04ER54698, Grant DE-FC02-99ER54512, Grant No. DE-FG032-04ER54758, Contract No. DE-SC04-94AL85000 and a Collaborative Research Opportunities grant from the Natural Sciences and Engineering Research Council of Canada.

Appendix: Obtaining I_{wall} from plasma measurements

The goal is to measure total ion flux, I_{wall}, received at the axisymmetric surfaces of the LFS main-wall, i.e. the window-frames (Figs 1-3). Direct measurements of received ion fluxes with embedded Langmuir probes are not typically available on main-wall surfaces. Therefore, we must derive I_{wall} from available plasma measurements of n_e and T_e on flux surfaces intercepting the window-frame, taking into account the varying magnetic geometry and the decrease of density along the flux surface due to the particle sink action of the window-frame.

The total ion current or sink at the window-frames, I_{wall} (ions s^{-1}), can be obtained by integrating the incident plasma flux density, Γ_i (ions s^{-1} m^{-2}), over the surface area of each of the window-frame "targets". Without loss of generality, we take the window-frame targets to be radial such that

$$I_{wall} = 2\pi \cdot \left[\int_{R_{window-pane}}^{R_\infty} \Gamma_i \, R \, dR \right]_{t,1} + 2\pi \cdot \left[\int_{R_{window-pane}}^{R_\infty} \Gamma_i \, R \, dR \right]_{t,2} , \qquad \text{(A1)}$$

where $R_{window\text{-}pane}$ to R_∞ represents the radial extent of the window-frame to all flux surfaces behind the window-pane, and each window-frame target (*t*) is arbitrarily labeled by the *t,1* or *t,2* subscript. At each target, Γ_i is related to the incident parallel ion flux density, $\Gamma_{i,//} = \Gamma_i \cdot (B_T/B_Z)$ by the magnetic pitch, B_Z/B_T where B_Z and B_T are the vertical and toroidal magnetic fields respectively. From the Bohm criterion, the plasma exhausts to the target at the sound speed, c_s (m s^{-1}), giving,

$$\Gamma_i = \left(\Gamma_{i,//} \frac{B_Z}{B_T} \right)_t = \left(n_e \, c_s \frac{B_Z}{B_T} \right)_t . \qquad \text{(A2)}$$

In the absence of measurements of T_i, we assume far SOL and shadowed flux surfaces to be isothermal, i.e. $T = T_e = T_i$. The plasma sound speed is evaluated from these temperatures [25]. Then Eq. A2 can be re-evaluated using plasma measurements of n_e and T_e at a reference position *O* distant from the window-frame target but residing on the same flux surface;

$$\Gamma_i = \left(\frac{n_{e,t}}{n_{e,O}} \right) n_{e,O} \left(\frac{kT_e + kT_i}{m_i} \right)^{1/2} \left(\frac{B_z}{B_T} \right)_t = \xi \, n_{e,O} \left(\frac{2kT}{m_i} \right)^{1/2} \left(\frac{B_z}{B_T} \right)_t , \qquad \text{(A3)}$$

where m_i is the plasma ion mass, k is the Boltzman's consant and the *O* subscript denotes parameters measured at position *O*.

In Eq. A3 the factor $\xi \equiv n_{e,t} / n_{e,o}$ is defined as the ratio of the density at the window-frame "target", $n_{e,t}$ to the density at the measurement point, *O*, typically at or near the outer midplane. We evaluate ξ using conservation of particles and momentum as in the "simple SOL" model in [25]. An added complication here is that the shadow plasma in tokamaks usually extends over regions of varying major radius, R, thereby changing the cross-sectional area of the flux bundles $A_{//} \propto 1/B \sim 1/B_T \propto R$, from the measurement point to the window-frame target. We will see that the changing area has a relatively weak effect on ξ, but calculate its effect for completeness.

Conservation of particles gives,

$$\frac{d(nvA_{//})}{ds} = SA_{//} \ , \qquad \text{(A4)}$$

and conservation of momentum gives,

$$m_i nv \frac{dv}{ds} = -\frac{dp}{ds} - m_i vS \ , \qquad \text{(A5)}$$

where S is the plasma source density (ion s^{-1} m^{-3}), v is the plasma velocity and p is the plasma pressure.

We define the Mach number, $M \equiv v / c_s$ and note that by definition a stagnation point, M=0, exists somewhere between the two window-frame targets. For convenience we choose the reference position *O* as the stagnation point. Again using isothermal flux surfaces, Eqs. A4-A5 can be combined to find

$$\frac{dM}{dx} = \left(1 - M^2\right)^{-1} \cdot \left[\frac{S\left(1 + M^2\right)}{n\, c_s} - M\left(A_{//}^{-1} \frac{dA_{//}}{dx}\right)\right], \qquad \text{(A6)}$$

$$\text{and } \frac{dn}{dx} = \left(1 + M^2\right)^{-1} \cdot \left[-2nM \frac{dM}{dx} - M^2 n\left(A^{-1} \frac{dA_{//}}{dx}\right)\right]. \qquad \text{(A7)}$$

Normalized numerical integration of Eqs. A6-A7 provides the M and $n(s) / n_O$ profiles from the stagnation point to the target for arbitrary S(s) and $A_{//}(s)$. An example of a numerical solution is shown in Fig. 13 for the case of the source, S, being constant along s, and assuming the ratio of

$A_{//,t} / A_{//,O} = R_t / R_O = 0.75$, with $A_{//}$ linearly decreasing from the stagnation point to the target. Fig. 14 shows the solution for $\xi \equiv n_t / n_O$ with varying $A_{//,t} / A_{//,O}$ with spatially constant S.

An analytic solution can also be obtained for ξ by using a "three-point" model. Here we take the flux tube to be comprised of two distinct regions. In the first region we use a constant source, S, and flux-bundle area, $A_{//}$, extending from the stagnation point, O, (again presumably at or near the outer midplane) to a point *p*. In the second region, there is no further source, i.e. S=0, but the cross-sectional area decreases by an arbitrary amount from *p* to the target, *t*, so that by conservation of particles,

$$n_p M_p A_{//,p} = n_t M_t A_{//,t} = n_t A_{//,t} \quad . \tag{A8}$$

In the first, constant source/area region one can combine Eqs. A4-A5 to obtain

$$\frac{n_p}{n_O} = \frac{1}{1 + M_p^2} \quad . \tag{A9}$$

For the second no-source region one can combine Eqs. A4-A5 to obtain

$$\frac{dM}{M} = - \frac{dA_{//} / A_{//}}{1 - M^2} \quad , \tag{A10}$$

and integrating Eq. A10 from location p to t gives

$$\frac{A_{//,p}}{A_{//,t}} = M_p^{-1} e^{(M_p^2 - 1)/2} \quad . \tag{A11}$$

From Eqs. A8-A9 one obtains

$$\xi = \frac{n_t}{n_O} = \frac{M_p}{1 + M_p^2} \frac{A_{//,p}}{A_{//,t}} \quad , \tag{A12}$$

and since Eq. A11 defines $M_p (A_{//,p} / A_{//,t})$, we have ξ as a function of the specified ratio of areas $A_{//,p} / A_{//,t}$.

The results of the analytic three-point model are compared to the numerical results in Fig. 13 and Fig. 14. As expected, we find $\xi = 0.5$ for a flux tube with constant area, i.e. $A_{//,t} / A_{//,O} = 1$. For most practical applications of the window-frame technique in a tokamak, one finds, $0.5 < \xi < 0.6$. Since both derivations provide similar answers, we use the three-point model for DIII-D experiments; it is easily calculated and probably best describes the experimental situation, namely of a source of particles arising from cross-field transport that is localized near the outer

midplane. In general it is clear that the parallel density profiles are weakly dependent on our assumptions about plasma sources (transport vs. ionization) and their location in the shadow plasma. This arises from two conditions in the shadow plasma: 1) The constant and low T (< 10 eV) inhibits significant parallel heat conduction transport that can cause perturbing recycling conditions at the target and 2) The strong boundary conditions imposed by sound speed exhaust, M=1, at the targets.

In order to evaluate the integrals of Eq. A1 we characterize the density profile by a radial exponential decay length, λ_{shadow}, behind the window-pane. Since $\lambda_{shadow,t} << R_{window\text{-}pane}$, we can simplify the integral equations in Eq. A1 to,

$$\int_{R_{window-pane}}^{R_\infty} \Gamma_i \, R \, dR \cong \langle R \rangle \, \lambda_{shadow} \Gamma_i \big|_{window-pane,t} \cong \langle R \rangle \, \lambda_{shadow} \left| n_e \left(\frac{2kT}{m_i} \right)^{1/2} \right|_{window-pane,t} \qquad \text{(A13)}$$

where $\langle R \rangle$ is the average radius of the window-frame's "leading edge" and Γ, n, T are window-pane plasma parameters as would be measured at the target. Since c_s profiles are not directly measured, we have made the reasonable simplification of taking λ_{shadow} from only n_e profiles, rather than from n_e c_s profiles, This does not introduce a significant error in I_{wall}: the n_e e-folding distance is ~4 times shorter than the decay length of $T_e^{1/2}$ (Fig. 5) and it is likely that T_i has an even weaker radial decay than T_e due to the poor collisional coupling between ions and electrons in the far SOL

Combining Eqs. A1, A3 and A13 we obtain,

$$I_{wall} \cong 2\pi \left[n_e \left(\frac{2kT}{m_i} \right)^{1/2} \right]_{window-pane,O} \left\{ \left(\xi \frac{B_z}{B_T} \lambda_{shadow} \langle R \rangle \right)_{t,1} + \left(\xi \frac{B_z}{B_T} \lambda_{shadow} \langle R \rangle \right)_{t,2} \right\} \qquad \text{(A14)}$$

where n_e and T are now measured at the stagnation point (*O*) on the window-pane flux surface. Eq. A14 can be further simplified by noting that (B_Z/B_T) λ_{shadow} is a conserved quantity on a poloidal flux surface and that the two window-frame targets are linked by the same flux surfaces. Therefore, we can finally obtain I_{wall} in a more convenient form,

$$I_{wall} \cong 2\pi \left[n_e \left(\frac{2kT}{m_i} \right)^{1/2} \right]_{window-pane,O} \left(\frac{B_Z}{B_T} \lambda_{shadow} \right)_O \left\{ \left(\xi \langle R \rangle \right)_{t,1} + \left(\xi \langle R \rangle \right)_{t,2} \right\}. \qquad \text{(A15)}$$

The form is most convenient because its evaluation exploits the typical practice of mapping SOL plasma profiles to the outer midplane, a convenient choice for the stagnation point, O. The first bracketed term of Eq. 15 is obtained by the fitting of SOL n_e and T_e at the outer midplane's window-pane flux surface. The second bracketed term uses outer midplane fits of radial density profiles into the shadow plasma and the outer midplane magnetic geometry. The third bracketed term is purely "geometrical" and is calculated based on the location of the window-frame targets (Eqs. A11-A12).

Case	$L_{//}$ m	λ_{shadow} mm	D_{eff} $m^2 s^{-1}$	v_{eff} $m s^{-1}$
L-Mode (Fig. 7)	14	30-40	3-6	110-140
H-Mode (Fig. 9)	20	40-60	4-9	100-150

Table 1 Summary of transport analysis based on λ_{shadow}.

Shot	$\delta_{W.F.}$ (mm)	λ_{shadow} mm	I_{wall} ions s^{-1}	Γ_i m^{-2} s^{-1}	$I_{div,\ LFS}$ ions s^{-1}	$f_{wall.}$	Q_{wall} / P_{div}
105194	60	29	5.5×10^{21}	0.7×10^{20}	5×10^{22}	0.11	0.04
105199	25	28	2.1×10^{22}	2.7×10^{21}	3.9×10^{22}	0.5	0.27
Change	***2.4***	***~ 1***	***× 3.8***	***× 4***	***× 0.78***	***× 5***	***× 7***

Table 2 Comparison of ion fluxes with decreasing gap distance between the separatrix and window-frame, $\delta_{W.F}$. Γ_i (= $\Gamma_{\iota,//}$ B_Z/B_T) is incident ion flux density at the embedded window-frame probe (Figs. 1-3). Q_{wall} / P_{div} is the ratio of conducted heat flux to the main-wall (Section 3.6) to the total power into the divertor ($P_{rad,div}$ + Q_{div}). Case shown is L-mode with $\bar{n}$ ~ $3.6\text{x}10^{19}$ m^{-3} (#105194, $\delta_{W.F.}$~60 mm in Fig. 7).

Figure Captions

Fig. 1

Typical DIII-D lower single null plasma geometry (R=1.7 m, a=0.6 m) and diagnostic locations. The thick dashed line marks the poloidal location of the toroidally continuous surface of the "window-frame" (δ~60 mm) flux surface through which cross-field plasma ion transport to the main-wall is measured for this shape. The intercepting upper and lower divertor baffle structures (labeled 'A' and 'B') are axisymmetric, and define the primary window-frame The surfaces defining the window-frame are labeled A and B. Note that the outer midplane wall is not axisymmetric (top view inset).

Fig. 2

A photograph of the DIII-D vessel interior showing the baffle surfaces used for the window-frame. Point 'A' and 'B' as defined in Fig. 1.

Fig. 3

A two-dimensional (// to B vs. δ) layout of the DIII-D SOL, shadow plasma, wall geometry and diagnostic locations. The axisymmetric surfaces defining the primary window-frame are labeled 'A'and 'B'. The secondary window-frames are defined by non-symmetric surfaces near the outer midplane. The relative scale of radial to parallel distance, ~ 1:1000 is greatly exaggerated for viewing clarity.

Fig. 4

An idealized schematic of the window-frame technique (see Appendix) for measuring plasma contact at the main-wall. (a) Radial transport, j_{wall}, carries plasma through the toroidally symmetric window-pane, where it undergoes both radial and parallel transport in the shadow region, which extends here indefinitely in the radial, r, direction. This establishes a radial density profile of characteristic length λ_{shadow}, neglecting any ionization sources in the shadow region. (b) Incident plasma flux occurs through a sheath to the baffle surfaces. A single embedded Langmuir probe is used to verify incident ion flux density at the baffle (Fig. 6).

Fig. 5

SOL profiles mapped to the outer midplane during an L-mode $\bar{n}$ scan. Shown are fits to Thomson scattering (TS) data of T_e (a) and n_e (b). Scanning probe T_e (c) and n_e (d) in the near and far SOL, with weighted fits to shadow plasma (shaded area) exponential decay length λ_{shadow}. Probe n_e has been multiplied by ~1.3 to normalize to TS n_e values in the SOL. The probe n_e profiles in (d) have the same relative scale but have been separated for viewing clarity. Vertical arrows mark T_e (a) and n_e (b) at δ~25 mm used to study effect of decreasing separatrix to window-frame gap (Table 2).

Fig. 6

The predicted incident parallel ion flux density, $\Gamma_{i,//} = \xi\, n_e\, c_s$, based on n_e and T_e measured in the shadow plasma (see Appendix), is compared to the direct measurements of $\Gamma_{i,//}$, from an embedded Langmuir probe in the upper-baffle window-frame (Fig. 1) . The flux surface location, δ, of the measurement and shadow plasma diagnostic are noted. The comparison shows good agreement in both L-mode and rapidly ELMing H-mode density scans.

Fig. 7.

Strength of various ion sinks at the main-wall, I_{wall}, and divertor are shown vs. line-averaged density for plasma geometry / SOL profiles as shown in Figs. 1 and 4. Ion losses to both surfaces (on the low-field side, and high-field side, HFS), and by divertor volume recombination are shown. The data are from discharges with L-mode energy confinement except as noted (attached ELMy H-mode). I_{wall} increases proportional to $\bar{n}^3$ in L-mode, while fitted λ_{shadow} (Fig. 4) is relatively constant vs. $\bar{n}$.

Fig. 8

Incident ion flux density Γ_ι ($=\Gamma_{\iota,//}\, B_Z/B_T$) vs. time, at the upper baffle (location A in Fig. 1) measured by the fixed embedded probe, is compared to Γ_D , the local D recycle influx based on D-α. The comparison is during a discharge that has L-mode and type-I ELMy H-mode phases. The probe position and D-α view/baffle intercept are on the δ~70 mm flux surface. (a) Comparison through L vs. H transitions (b) Correlated large increases in ion flux and main-wall recycling caused by type-I ELMs.

Fig. 9

Main-wall plasma contact during a core density scan with a rapidly ELMing H-mode plasma. (a) The H_{89} energy confinement scaling (1 ≡ L-Mode, 2 ≡ H-mode). (b) LFS ion losses to main-wall surfaces and divertor. (c) λ_{shadow} measured by TS. Inset shows upper single null plasma geometry used. The axisymmetric surfaces defining the window-frame are labeled A and B. Outer divertor detachment starts at $\bar{n} \sim 8 \times 10^{19}$ m^{-3}.

Fig. 10

Local influx of neutrals, Γ_D, inferred from D-α and pressure gauges located at various main chamber locations (Fig. 1), are compared to j_{wall} measured with the window-frame technique for the L-mode core density scan of Fig. 7. Local flux densities correlate well with j_{wall} but can vary in absolute magnitude by a factor of ten. The magnitude of D-α LFS upper baffle, (viewchord ending at "A" in Fig.1) was obtained by cross-calibration to a lower divertor D-α signal on another shot w, with the cross-calibration verified by comparing local ion fluxes from probes.

Fig. 11

Power input and losses in L-mode core density scan (Fig. 7). Consistent with power balance, the power lost to the main-wall chambers via plasma-wall interaction (i.e. through a sheath), $Q_{wall} \sim 6\ k\ T_e\ I_{wall}$ increases with n_e while Q_{div} vanishes at high $\bar{n}$ due to detachment.

Fig. 12

Carbon radiation pattern during L-mode core density scan (Fig. 7). a) Divertor and main-wall ion fluxes (Fig. 7) versus $\bar{n}$ line average density. b) Visible $C^{=2}$ (465 nm) from the lower divertor, upper baffle knee and outer midplane. c) Total radiated power from bolometers for the outer divertor leg and top SOL near the upper baffle. Insets shows poloidal views with shading that matches data points in b) and c).

Fig. 13

Solutions for the profiles of density, n and Mach number flow, M, along a flux surface when the cross-sectional area, A, decreases by 25% from the stagnation point or midplane to the window-

frame target. Lines are numerical solutions for the case of a constant source, S, along the flux surface. The symbols show the results of the analytic three-point model.

Fig. 14

Solutions for ξ, the ratio of target density, n_t to stagnation point density, n_O, versus A_t / A_O , the ratio of the flux surface's cross-sectional areas at the target, A_t to the stagnation point A_O. Solutions for both the numerical and analytic three-point model are shown. The area ratio A_t / A_O is approximately equal to the ratio of the major radii at each location since $A \sim 1/B \sim R$.

References

[1] I.H. Hutchinson, R. Boivin, F. Bombarda *et al.*, Phys. Plasmas **1**, 1511 (1994).
[2] M. V. Umansky, S. I. Krasheninnikov, B. LaBombard *et al.*, Phys. Plasmas **5**, 3373 (1998).
[3] B. LaBombard, M. V. Umansky, R. L. Boivin *et al.*, Nucl. Fusion **40**, 2041 (2000).
[4] B. LaBombard and B. Lipschultz, "Cross-field transport in the SOL: Its relationship to main chamber and divertor neutral control in Alactor C-Mod", presented at the 18th IAEA Fusion Energy Conference, Sorrento, Italy, 2000, IAEACN-77, EX5/6, (2000).
[5] L. Rudakov, J. A. Boedo, R. A. Moyer *et al.*, Plasma Phys. Controlled Fusion **44(6)**, 717 (2002).
[6] S.I. Krasheninnikov, Phys. Lett. A **283**, 368 (2001).
[7] B. LaBombard, Phys. Plasmas **9(4)**, 1300 (2002).
[8] M. Endler, J. Nucl. Mater. **266-269**, 84 (1999).
[9] J. A. Boedo, D. Rudakov, R. Moyer *et al.*, Phys. Plasmas **8**, 4826 (2001).
[10] S. J. Zweben, D. P. Stotler, J. L. Terry *et al.*, Phys. Plasmas **9**, 1981 (2002).
[11] G.R. Tynan, L. Schmitz, R.W. Conn *et al.*, Phys. Rev. Lett. **68**, 3032 (1992).
[12] B. Lipschultz and D. G. Whyte, Companion paper (2004).
[13] P. C. Stangeby, Phys. Plasmas **9**, 3489 (2002).
[14] J.L. Luxon, Nucl. Fusion **42**, 614 (2002).
[15] H. S. Bosch, J. Neuhauser, R. Schneider *et al.*, J. Nucl. Mater. **220-222**, 558 (1995).
[16] A. Yu Pigarov, S. I. Krasheninnikov, W. P. West *et al.*, J. Nucl. Mater. **313-316**, 1076 (2003).
[17] C.S. Pitcher and P.C. Stangeby, Plasma Phys. Controlled Fusion **39**, 779 (1997).
[18] C.L. Hsieh, R. Chase, J.C. DeBoo *et al.*, Rev. Sci. Instrum. **59**, 1467 (1988).
[19] J.G. Watkins, J. Salmonson, R. Moyer *et al.*, Rev. Sci. Instrum. **63**, 4728 (1992).
[20] J. G. Watkins, P. Stangeby, J. A. Boedo *et al.*, J. Nucl. Mater. **290-293**, 778 (2001).
[21] D. Reiter and A. Nicolai, J. Nucl. Mater. **128-129**, 458 (1984).
[22] J. L. Terry, B. Lipschultz, X. Bonnin *et al.*, J. Nucl. Mater. **266-269**, 30 (1999).
[23] S. Lisgo, P. Stangeby, J. D. Elder *et al.*, J. Nucl. Mater., accepted for publication (2004).
[24] A. W. Leonard, J. A. Boedo, M. E. Fenstermacher *et al.*, J. Nucl. Mater. **313-316**, 768 (2003).
[25] P. C. Stangeby, *The plasma boundary of magnetic fusion devices*. (Institute of Physics Pub., Bristol ; Philadelphia, 2000).
[26] J. A. Boedo, D. L. Rudakov, R. A. Moyer *et al.*, Phys. Plasmas **10(5)**, 1670 (2003).
[27] L.C. Johnson and E. Hinnov, Journal of Quantitative Spectroscopy and Radiative Transfer **13**, 333 (1973).
[28] M. Groth, L. W. Owen, G. D. Porter *et al.*, J. Nucl. Mater., accepted for publication (2004).
[29] R. J. Colchin and L. W. Owen, J. Nucl. Mater. **313-316**, 609 (2003).
[30] B. Lipschultz, P. Andrew, J. Coad *et al.*, "A study of JET radial transport based on particle balance", presented at the 30th European Conf. On Controlled Fusion and Plasma Physics, St. Petersburg, Russia, 2003, (2003).
[31] ITER Technical Basis, Report No. G A0 FDR 4 01-07-21 R 0.4, 2001.
[32] D.G. Whyte and R.P. Doerner, Physica Scripta **T91**, 7 (2001).

[33] G. Janeschitz, R. Konig, L. Lauro-Taroni *et al.*, J. Nucl. Mater. **196-198**, 380 (1992).
[34] G. M. McCracken, R. S. Granetz, B. Lipschultz *et al.*, J. Nucl. Mater. **241-243**, 777 (1997).
[35] B. Lipschultz, D.A. Pappas, B. Labombard *et al.*, Nucl. Fusion **41**, 585 (2001).
[36] J. D. Strachan, K. Erents, W. Fundamenski *et al.*, J. Nucl. Mater. **290-293**, 972 (2001).
[37] W. P. West, C. J. Lasnier, D. G. Whyte *et al.*, J. Nucl. Mater. **313-316**, 1211 (2003).
[38] D.G. Whyte, W.P. West, C.P.C. Wong *et al.*, Nucl. Fusion **41**, 1243 (2001).
[39] M. Ali Mahdavi, J.C. DeBoo, C.L. Hsieh *et al.*, Phys. Rev. Lett. **47**, 1602 (1981).
[40] M. Keilhacker, K. Lackner, K. Behringer *et al.*, Physica Scripta **T2**, 443 (1982).

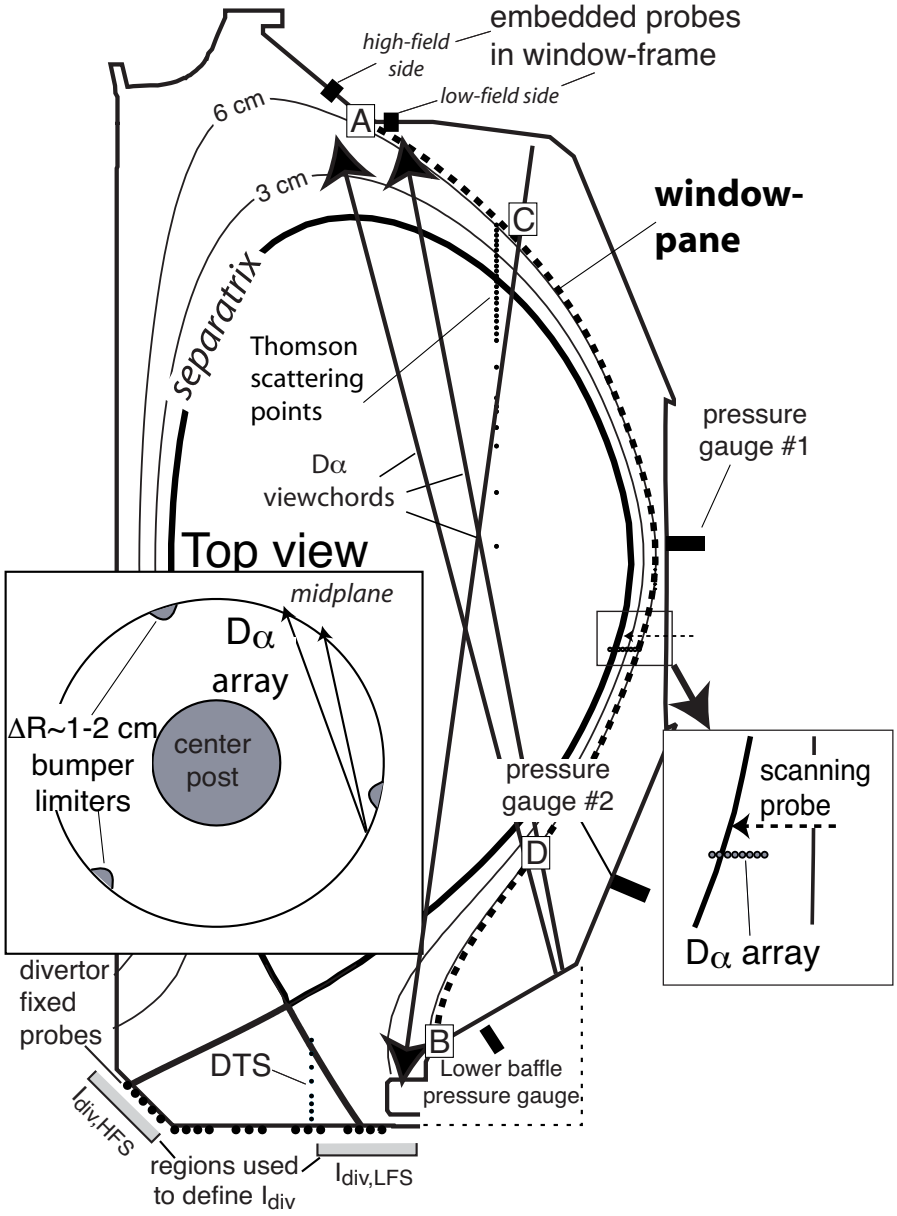
embedded probes
in window-frame
high-field
side
low-field side
6 cm
3 cm
A
C
window-
pane
separatrix
Thomson
scattering
points
pressure
gauge #1
Dα
viewchords
Top view
midplane
Dα
array
ΔR~1-2 cm
bumper
limiters
center
post
pressure
gauge #2
D
scanning
probe
Dα array
divertor
fixed
probes
DTS
B
Lower baffle
pressure gauge
Idiv,HFS
regions used
to define Idiv
Idiv,LFS

Figure 1

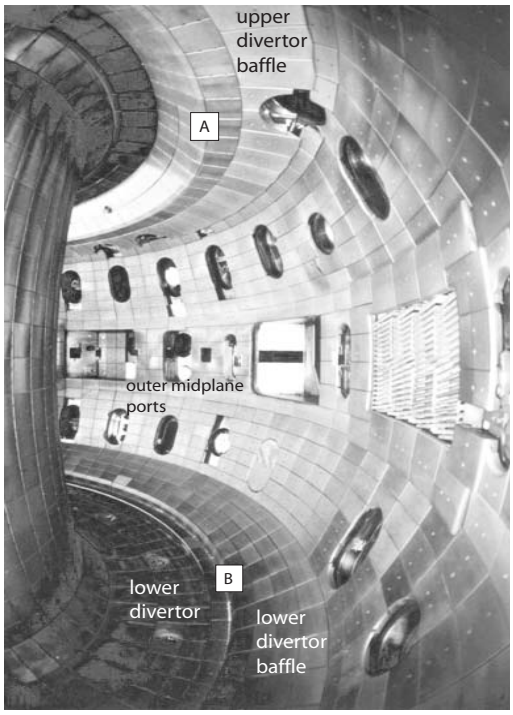
upper
divertor
baffle
A
outer midplane
ports
B
lower
divertor
lower
divertor
baffle

Figure 2

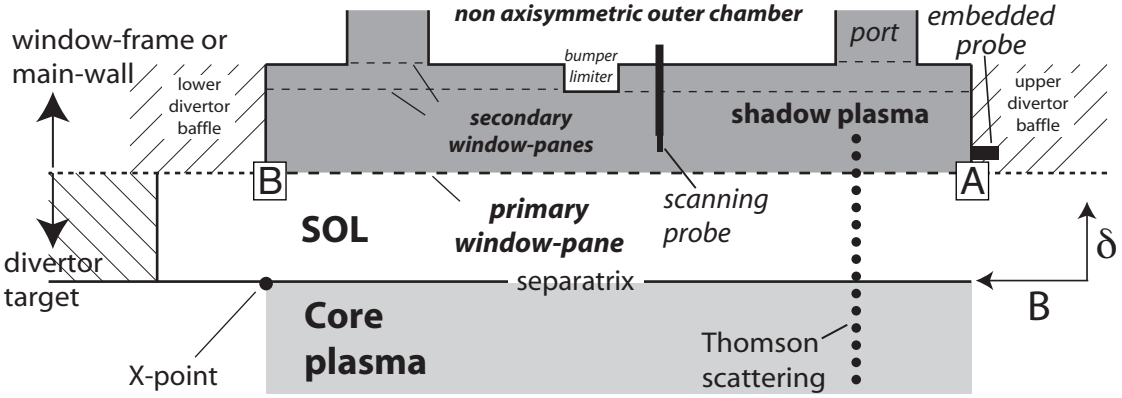
non axisymmetric outer chamber
port
embedded probe
window-frame or main-wall
bumper limiter
lower divertor baffle
upper divertor baffle
secondary window-panes
shadow plasma
B
A
SOL
primary window-pane
scanning probe
δ
divertor target
separatrix
B
Core plasma
Thomson scattering
X-point

Figure 3

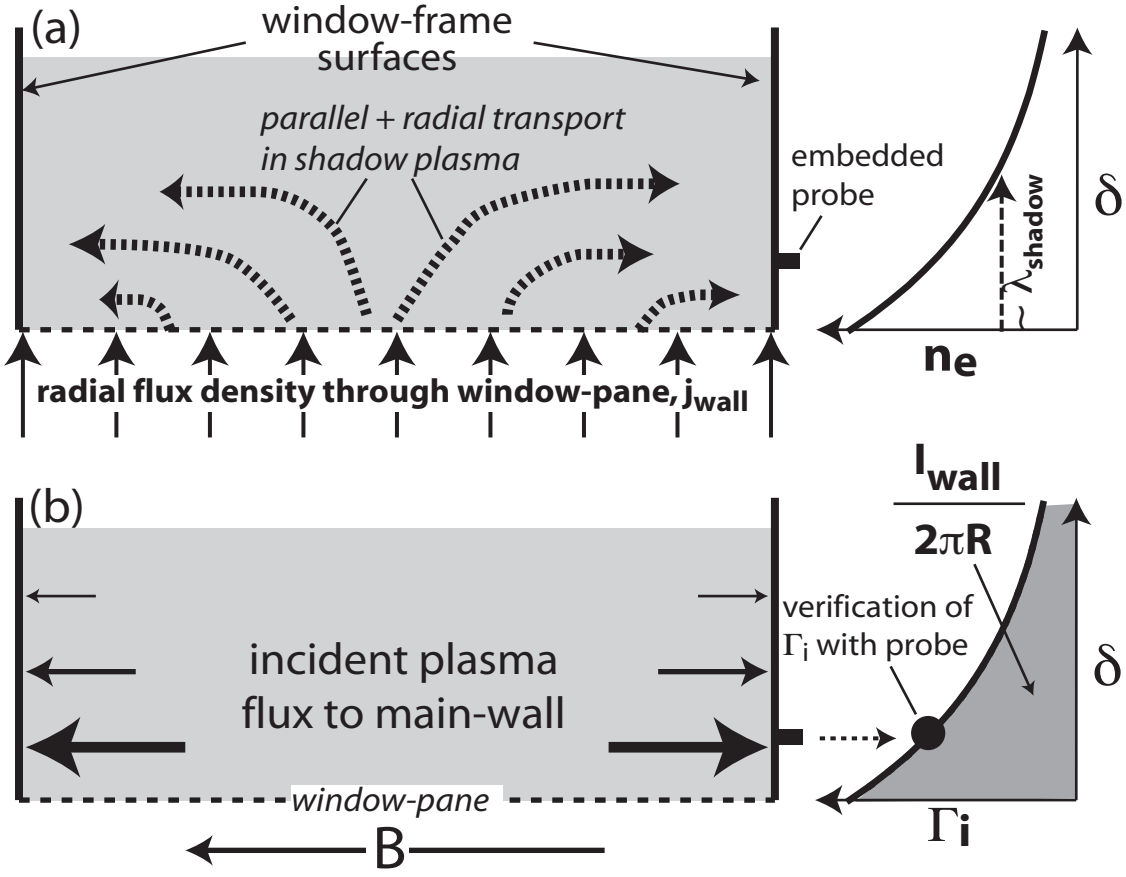
(a)
window-frame surfaces
parallel + radial transport in shadow plasma
embedded probe
δ
λshadow
ne
radial flux density through window-pane, jwall
(b)
Iwall
2πR
verification of Γi with probe
δ
incident plasma flux to main-wall
window-pane
B
Γi

Figure 4

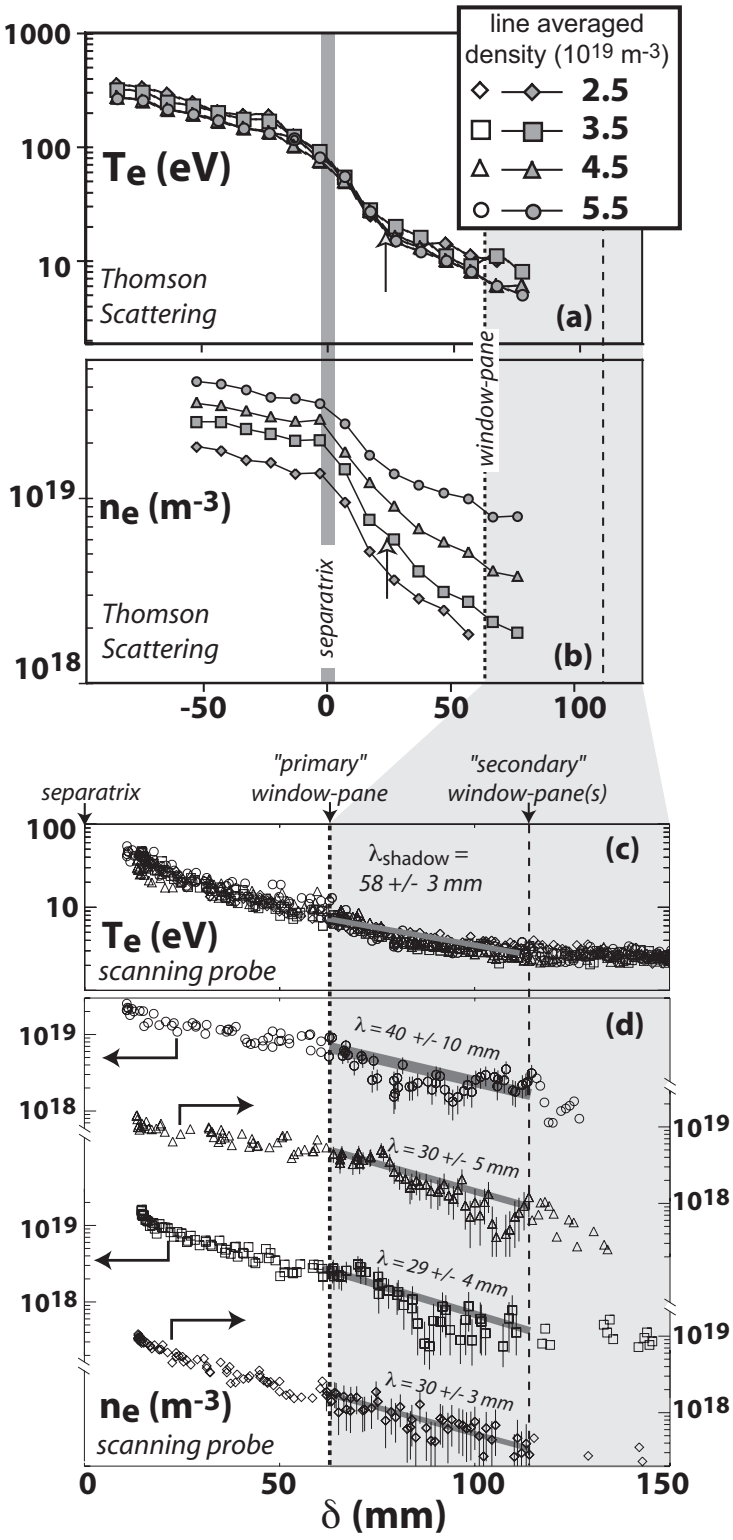
line averaged
density (10^19 m^-3)
2.5
3.5
4.5
5.5
1000
100
10
Te (eV)
Thomson
Scattering
(a)
window-pane
10^19
10^18
ne (m^-3)
Thomson
Scattering
separatrix
(b)
-50
0
50
100
separatrix
"primary"
window-pane
"secondary"
window-pane(s)
100
10
λshadow =
58 +/- 3 mm
(c)
Te (eV)
scanning probe
10^19
10^18
λ = 40 +/- 10 mm
(d)
λ = 30 +/- 5 mm
λ = 29 +/- 4 mm
λ = 30 +/- 3 mm
ne (m^-3)
scanning probe
0
50
100
150
δ (mm)

Figure 5

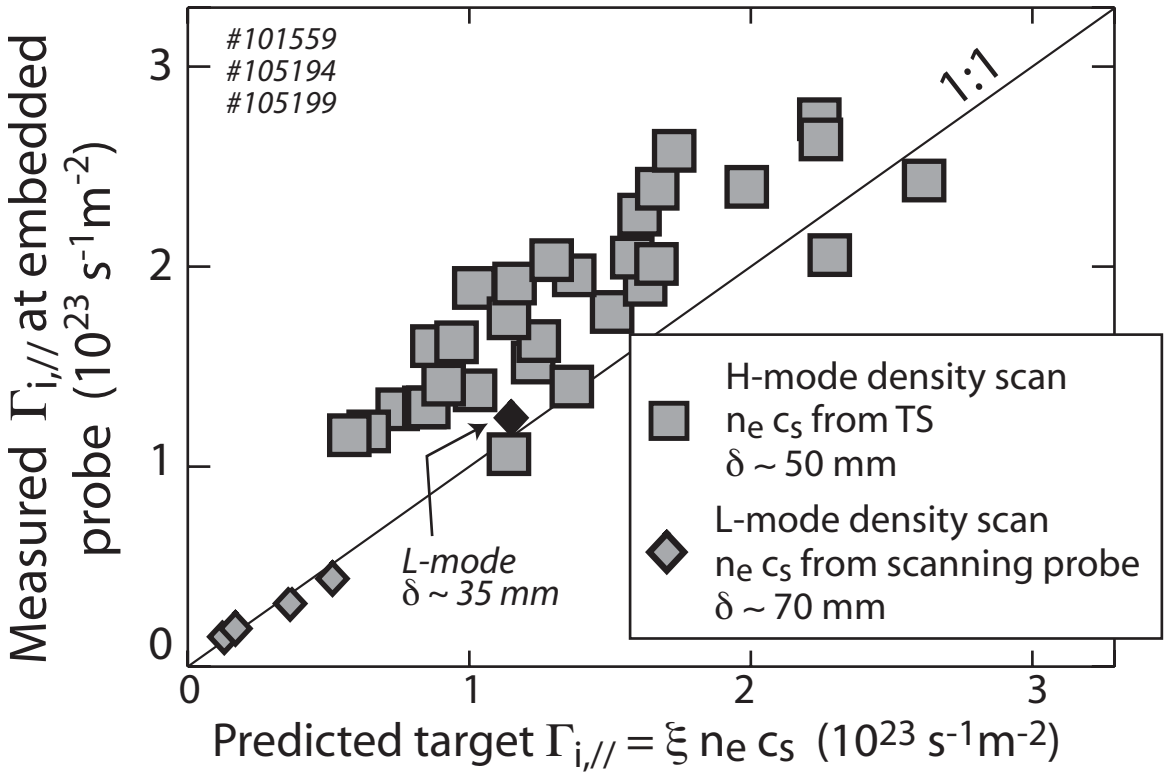
#101559
#105194
#105199
1:1
H-mode density scan
n_e c_s from TS
$\delta \sim 50$ mm
L-mode density scan
n_e c_s from scanning probe
$\delta \sim 70$ mm
L-mode
$\delta \sim 35$ mm
Measured $\Gamma_{i,//}$ at embedded probe (10^{23} $s^{-1}m^{-2}$)
Predicted target $\Gamma_{i,//} = \xi\, n_e\, c_s$ (10^{23} $s^{-1}m^{-2}$)
0
1
2
3

Figure 6

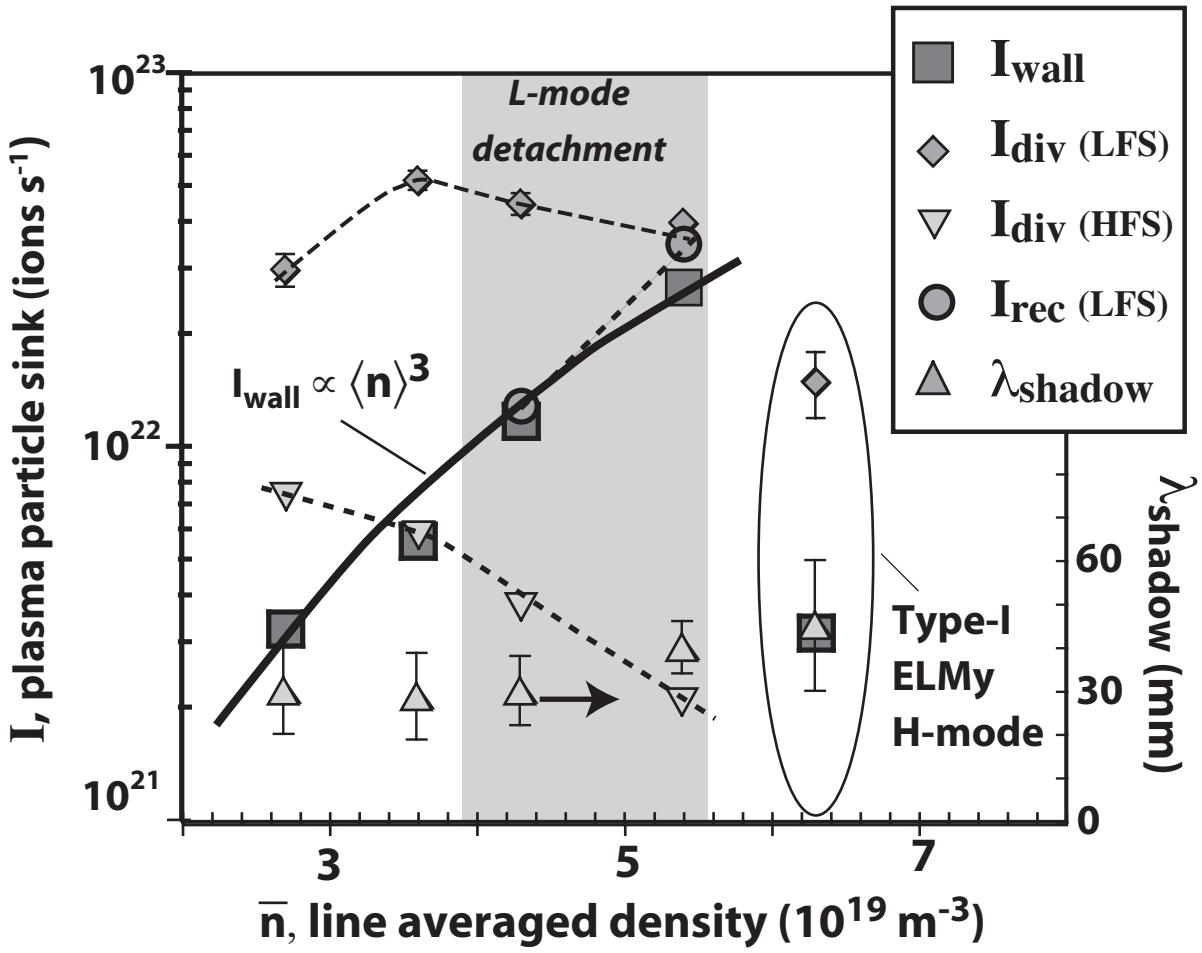
I_{wall}
I_{div} (LFS)
I_{div} (HFS)
I_{rec} (LFS)
λ_{shadow}
L-mode
detachment
$I_{wall} \propto \langle n \rangle^3$
Type-I
ELMy
H-mode
10^{23}
10^{22}
10^{21}
I, plasma particle sink (ions s^{-1})
60
30
0
λ_{shadow} (mm)
3
5
7
$\bar{n}$, line averaged density (10^{19} m^{-3})

Figure 7

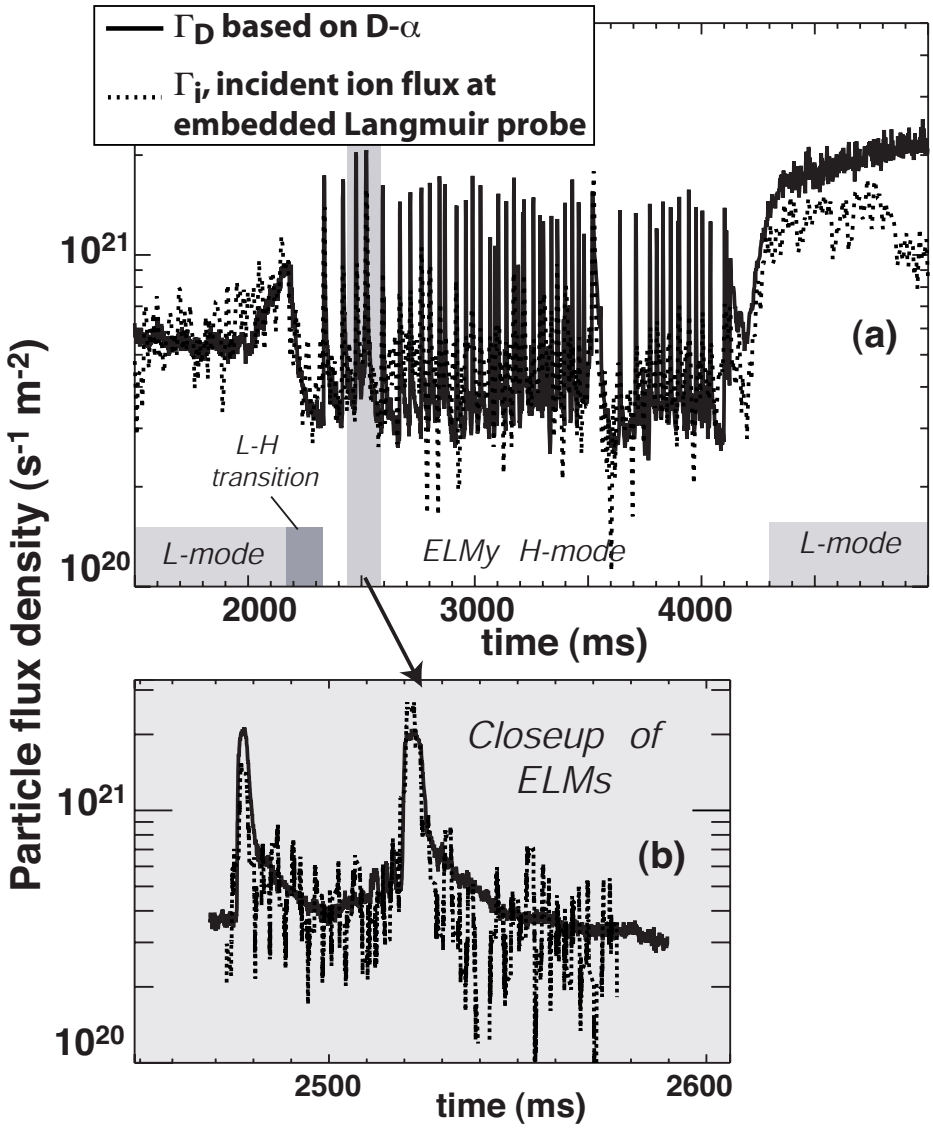
Γ_D based on D-α
Γ_i, incident ion flux at embedded Langmuir probe
Particle flux density (s^-1 m^-2)
10^21
10^20
(a)
L-H transition
L-mode
ELMy H-mode
L-mode
2000
3000
4000
time (ms)
Closeup of ELMs
(b)
10^21
10^20
2500
2600
time (ms)

Figure 8

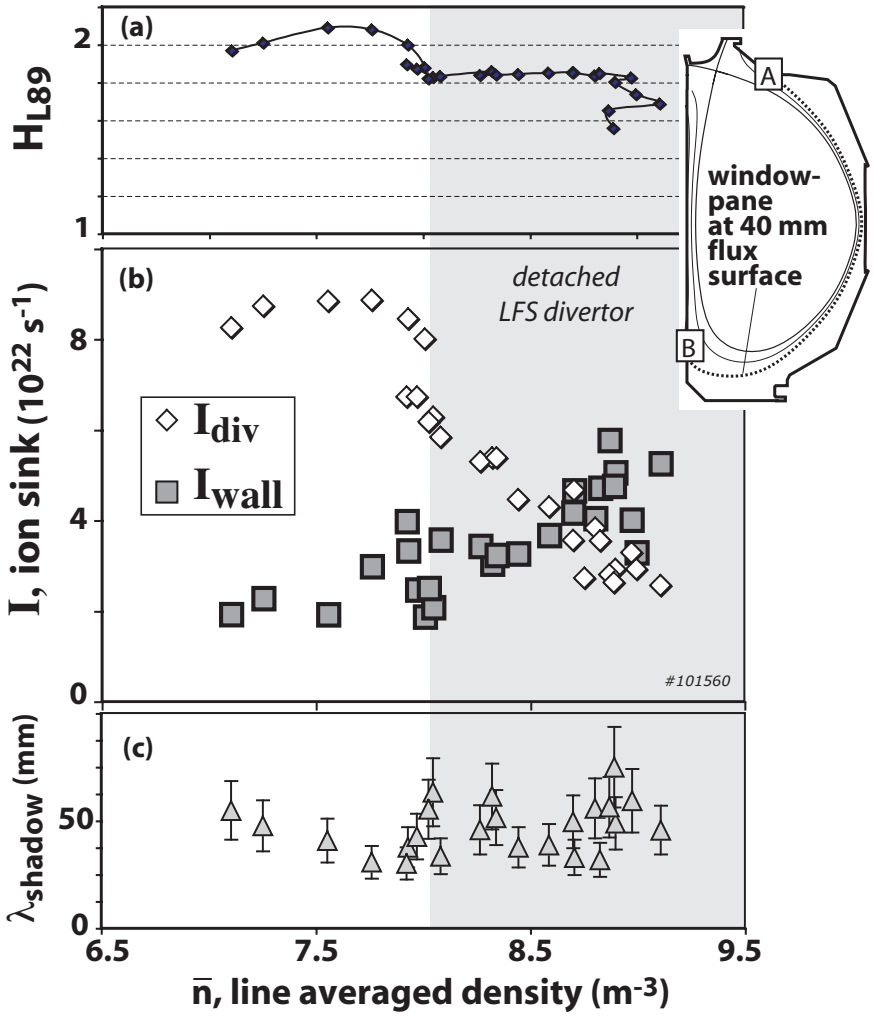
(a)
H_{L89}
2
1
(b)
detached
LFS divertor
I_{div}
I_{wall}
I, ion sink (10^{22} s^{-1})
8
4
0
#101560
(c)
λ_{shadow} (mm)
50
0
6.5
7.5
8.5
9.5
$\bar{n}$, line averaged density (m^{-3})
A
B
window-
pane
at 40 mm
flux
surface

Figure 9

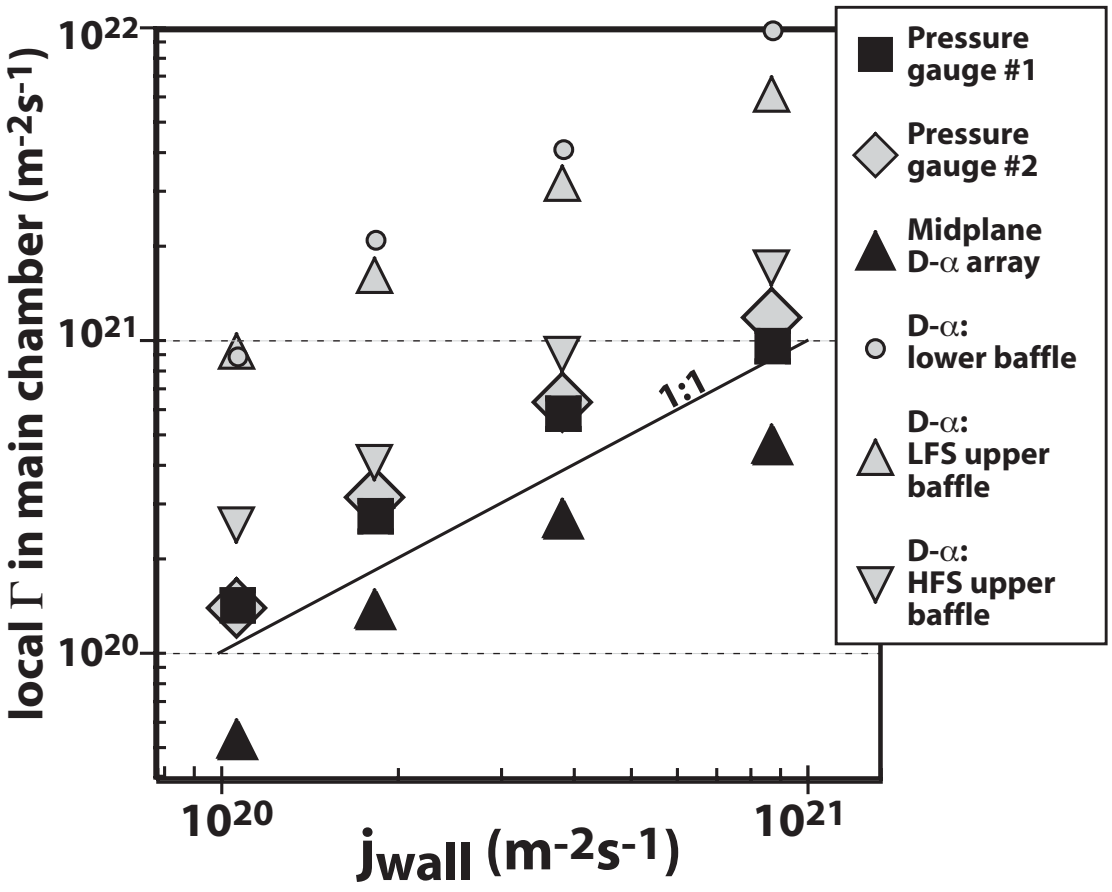
local Γ in main chamber (m-2s-1)
10^22
10^21
10^20
10^20
10^21
jwall (m-2s-1)
1:1
Pressure gauge #1
Pressure gauge #2
Midplane D-α array
D-α: lower baffle
D-α: LFS upper baffle
D-α: HFS upper baffle

Figure 10

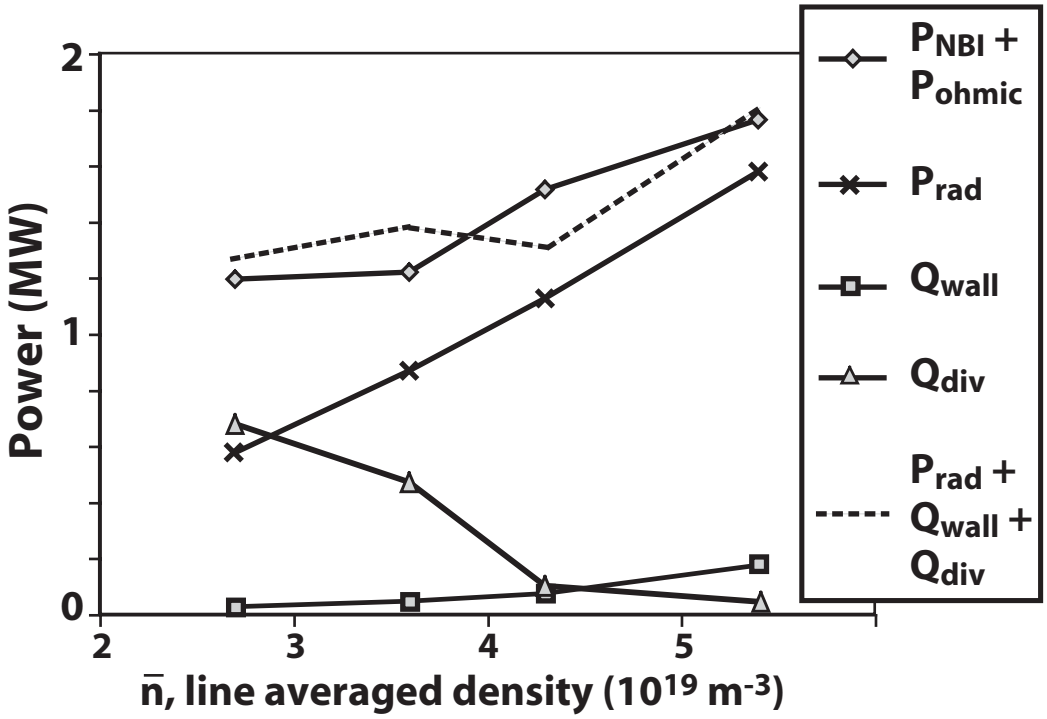
2
1
0
Power (MW)
2
3
4
5
n̄, line averaged density (10^19 m^-3)
P_NBI + P_ohmic
P_rad
Q_wall
Q_div
P_rad + Q_wall + Q_div

Figure 11

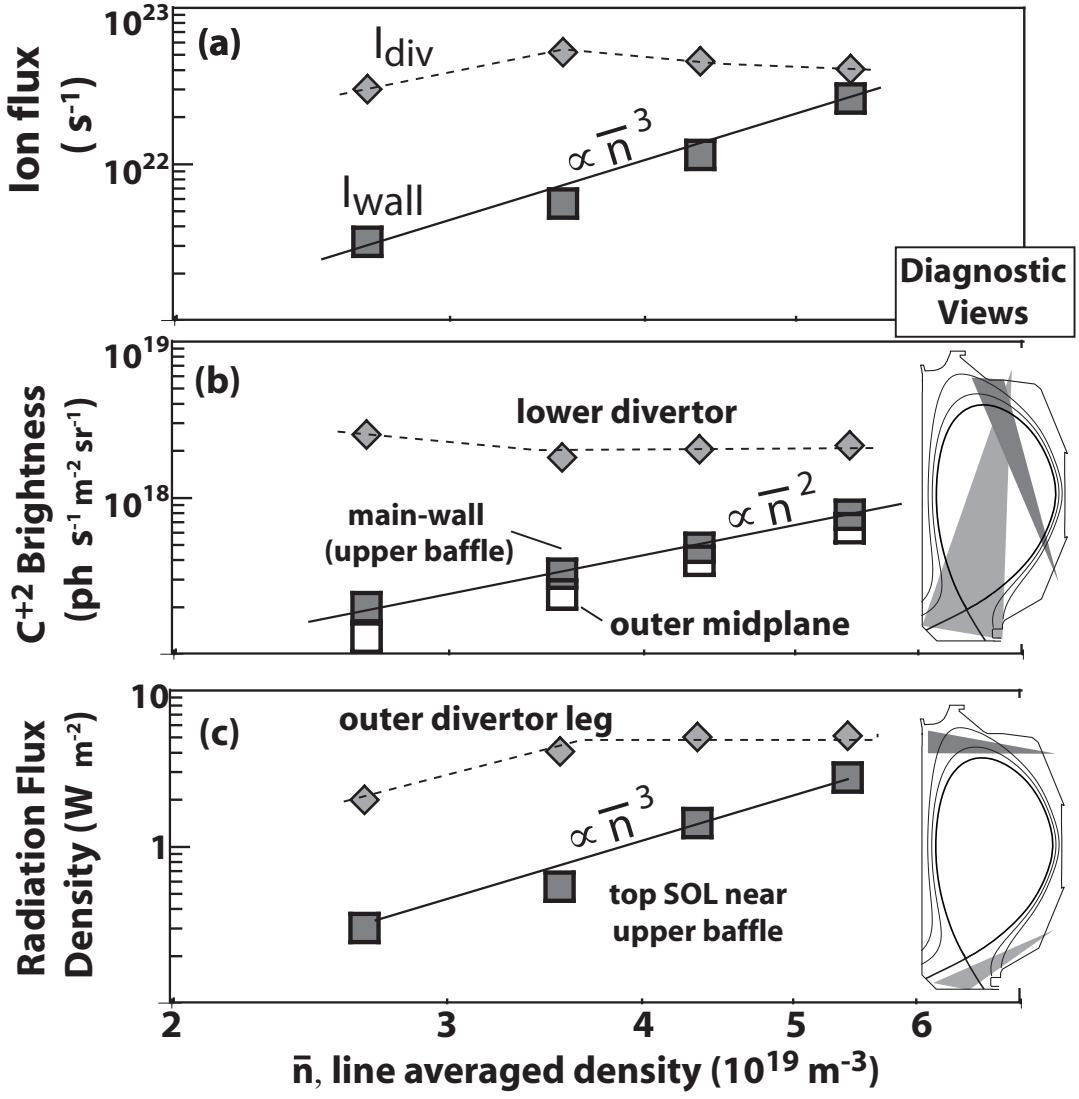
Ion flux (s-1)
10^23
10^22
(a)
I_div
I_wall
∝ n̄^3
Diagnostic Views
C+2 Brightness (ph s-1 m-2 sr-1)
10^19
10^18
(b)
lower divertor
main-wall (upper baffle)
∝ n̄^2
outer midplane
Radiation Flux Density (W m-2)
10
1
(c)
outer divertor leg
∝ n̄^3
top SOL near upper baffle
2
3
4
5
6
n̄, line averaged density (10^19 m^-3)

Figure 12

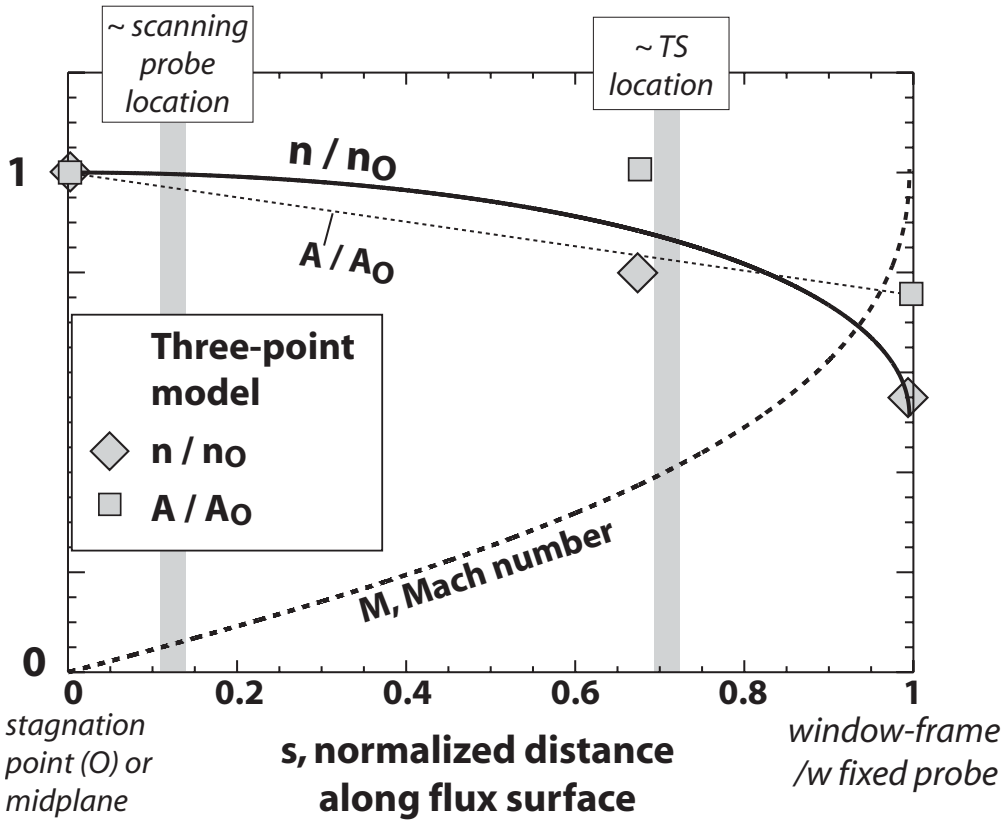
~ scanning probe location
~ TS location
1
n / nO
A / AO
Three-point model
n / nO
A / AO
M, Mach number
0
0
0.2
0.4
0.6
0.8
1
stagnation point (O) or midplane
s, normalized distance along flux surface
window-frame /w fixed probe

Figure 13

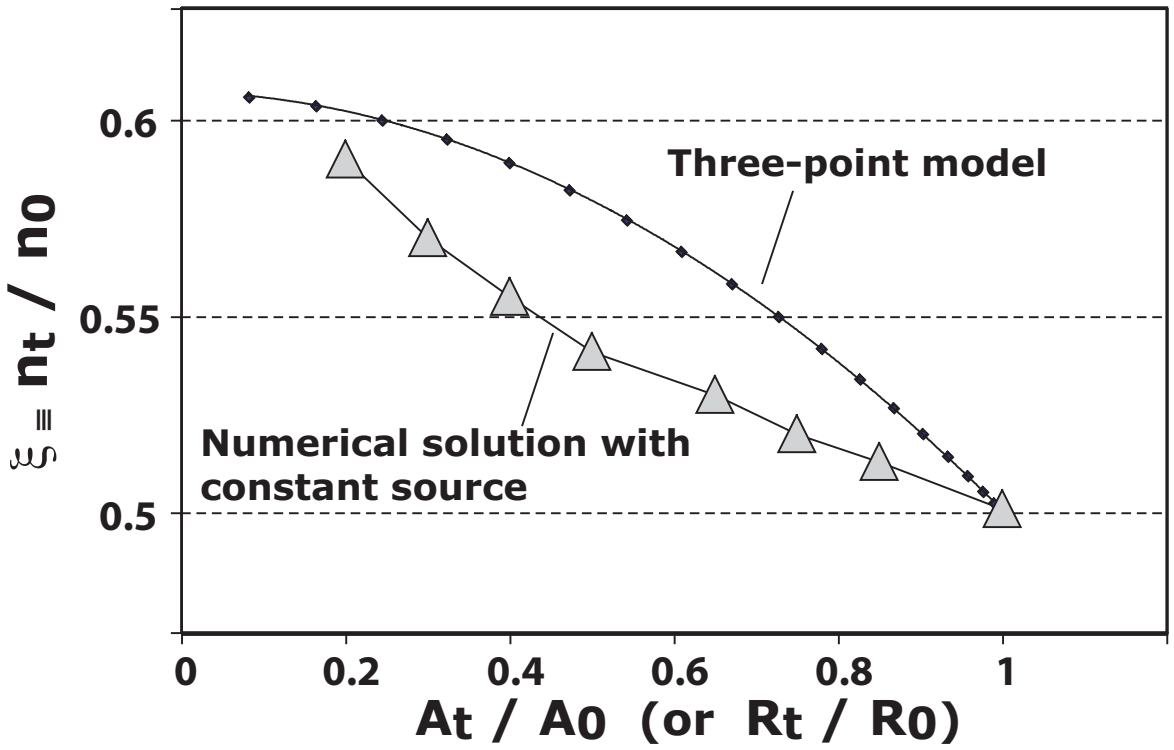
0.6
0.55
0.5
Three-point model
Numerical solution with
constant source
0
0.2
0.4
0.6
0.8
1
At / A0 (or Rt / R0)

Figure 14